Numerical analysis of small-strain elasto-plastic deformation using local Radial Basis Function approximation with Picard iteration

Filip Strniša, Mitja Jančič, Gregor Kosec *

"Jozef Stefan" Institute, Parallel and Distributed Systems Laboratory, Jamova cesta 39, Ljubljana, 1000, Slovenia

ARTICLE INFO

ABSTRACT

In this paper, we discuss a von Mises plasticity model with nonlinear isotropic hardening assuming small strains in a plane strain example of internally pressurised thick-walled cylinder subjected to different loading conditions. The elastic deformation is modelled using the Navier-Cauchy equation. In regions where the von Mises stress exceeds the yield stress, corrections are made locally through a return mapping algorithm. We present a novel method that uses a Radial Basis Function-Finite Difference (RBF-FD) approach with Picard iteration to solve the system of nonlinear equations arising from plastic deformation. This technique eliminates the need to stabilise the divergence operator and avoids special positioning of the boundary nodes, while preserving the elegance of the meshless discretisation and avoiding the introduction of new parameters that would require tuning. The results of the proposed method are compared with analytical and Finite Element Method (FEM) solutions. The results show that the proposed method achieves comparable accuracy to FEM while offering significant advantages in the treatment of complex geometries without the need for conventional meshing or special treatment of boundary nodes or differential operators.

1. Introduction

The study of plasto-elastic behaviour is a field of research concerned with the challenges associated with modelling the deformation of materials that exhibit both elastic and plastic behaviour under applied loads [1,2]. These materials, which are widely used in engineering and manufacturing, initially exhibit linear elastic behaviour when subjected to mechanical stress, but begin to deform plastically as soon as yield stress is exceeded. Accurate prediction of this transition is important for the design and analysis of structural components subjected to dynamic loads such as earthquakes, for modelling the behaviour of soils and rocks under construction loads or natural forces, and for additive manufacturing processes where materials are often subjected to complex loads, to name but a few applications.

There are various methods for modelling elastic deformation. The Euler-Bernoulli beam theory is a classical approach to model the mechanical behaviour of slender beams under load [3]. Euler-Bernoulli theory assumes that plane sections of the beam remain perpendicular to its neutral axis after deformation, neglecting shear deformation, making it well-suited for long, slender beams where shear effects are minimal. The Timoshenko beam theory [3] is an extension of the Euler-Bernoulli theory that incorporates both shear deformation and rotational effects, offering more accurate predictions for shorter, thicker, or more flexible beams. For further discussion on beam theories and their motivations, see [4]. To model the bending mechanics of thin elastic plates, the Kirchhoff-Love

---

* Corresponding author.
E-mail addresses: filip.strnisa@ijs.si (F. Strniša), mitja.jancic@ijs.si (M. Jančič), gregor.kosec@ijs.si (G. Kosec).

hypothesis [5,6] provides a simplified yet effective framework. This hypothesis disregards shear deformation, which is valid when the plate's thickness is small in comparison to its other dimensions. To achieve greater accuracy or handle complex materials, higher-order theories [7,8], such as the Sheremetev-Pelekh-Reddy-Levinson model [9], have been developed. However, at the micro-scale, where materials are assumed to behave isotropically, simpler 1D models like the Euler-Bernoulli theory have been shown to provide sufficient accuracy [10]. In this paper we will, however, focus on the general Navier-Cauchy theory of elasticity that deals with the deformation of 3D elastic bodies under arbitrary loading conditions.

As soon as the material begins yielding, the Navier-Cauchy solution is considered as an initial guess in an iterative algorithm that adjusts the solution locally. Traditionally, the Finite Element Method (FEM) is used to solve elasto-plastic problems [11–14]. Although FEM is a powerful tool that offers a mature and versatile solution approach including all types of adaptivities, well-understood error indicators [15] and an established toolset for Isogeometric Analysis (IGA), i.e. coupling with Computer-Aided Design (CAD) [16], the complexity of mesh generation has led researchers to explore alternative methods. In FEM, the domain is discretised by dividing a complex geometry into smaller, simpler parts, called finite elements, that cover it entirely. Despite significant developments in the field of mesh generation, the process of meshing often remains the most time-consuming part of the overall solution procedure. At the same time, the quality of the mesh has a direct impact on the accuracy, convergence and computational cost of the method.

In contrast, meshless methods work with clouds of nodes, which are often referred to as scattered nodes and do not require a topological relationship between them. Although some authors argued that arbitrary nodes could be used, it is nowadays generally accepted that the domain should be discretised with quasi-uniformly [17] distributed scattered nodes for a stable meshless approximation. Modern node positioning algorithms can automatically populate complex geometries, are dimension-independent, support variable node densities and can handle domains whose boundaries are defined by CAD objects [18–23], and are less complex than meshing [18].

Throughout the years, several meshless methods have emerged with popular techniques including the Finite Point Method [24], Smooth Particle Hydrodynamics [25], Meshless Local Petrov-Galerkin method [26], RBF partition of unity method [27], among others. This paper specifically explores a widely recognized method, a local Radial Basis Function-generated Finite differences (RBF-FD) [28] that has been gaining popularity in recent years. RBF-FD uses polyharmonic (PHS) RBFs augmented with monomials [29] to avoid stagnation errors and allow control over the convergence rate. In recent years the method has been extensively researched as well as applied to various problems [30–34].

In general, meshless methods have already been applied in elasto-plastic problems. In [35] authors demonstrated the Reproducing Kernel Particle Method weak solution of Drucker-Prager and Mohr-Coulomb models. Another weak form solution was presented in [36], where authors demonstrated the Element free Galerkin method in elasto-plastic stress analysis around the tip of a crack. In [37] a Radial Point Interpolation method was demonstrated in elasto-plastic analysis of frame structures.

In weak form methods, the governing equations of plasticity are formulated in an integral form rather than a differential form. The key difference from strong form meshless methods, which directly discretize the differential equations at nodes, is that weak form methods satisfy these equations in an average sense over the domain, hence potentially increasing the solution's smoothness and numerical stability. However, a recent study revealed that strong form solution might perform better in capturing the peaks in the stress comparing it to the weak from solutions [38].

In strong form, elasto-plastic deformation was simulated using the meshless Method of Fundamental Solutions (MFS) to model material undergoing plastic deformation, as characterized by the Chakrabarty model [39]. In the RBF-FD context, this problem was recently addressed in the analysis of cantilever beams and reinforced concrete column-steel systems [40]. The authors employed a multiquadratic basis, requiring shape tuning, which can significantly affect the numerical solution's accuracy due to stagnation errors and the stability of the solution procedure [29,41]. Their solution also stabilized the calculation of the first derivatives using the Finite Difference Method (FDM) on bilinear local nodes. However, as their study was limited to regular nodes, they only discussed extending the approach to scattered nodes by using fictitious nodes for interpolating the field nodes. This extension was properly implemented in a recent paper [42], where the authors argued that direct RBF-FD, without using FDM for the divergence operator, is unsuitable for solving elasto-plastic problems. Furthermore, they introduced stabilization of the boundary conditions by adding the first two layers of nodes inside the domain opposite the outward-facing normal vector instead of using purely scattered nodes. The authors also demonstrated that such stabilization is essential for the method's convergence.

In this paper, we present a novel approach using a pure RBF-FD with Picard iteration, which requires neither stabilisation of the divergence operator nor special positioning of the boundary nodes. The main advantage of such an approach is that the RBF-FD is used to approximate all involved operators on purely scattered nodes without the need for special treatment of boundary nodes nor special discretisation of any differential operator, which would reduce the elegance of the meshless discretisation and introduce new free parameters that need to be tuned. Consequently, the proposed approach can be directly applied to complex geometries and offers all the advantages of meshless discretisation. The proposed method is verified by analysing an internally pressurized thick-walled cylinder under small strains assumption in a plane strain approximation using the von Mises plasticity model under different loading conditions. These conditions induce states of elastic expansion, perfectly-plastic yielding and plastic yielding with linear hardening. The results are compared with analytical and FEM solutions. The paper also demonstrates the robustness of this approach by solving the case of a thick-walled cylinder with cut-outs. The results confirm that the proposed method produces outcomes comparable to those achieved using FEM. At the same time, it offers significant advantages in coping with complex geometries without the need for conventional meshing or special treatment of boundary nodes or any involved differential operator. This work extends the spectra of meshless solutions to plasticity problems as well as the application of Picard iteration to elasto-plastic materials, originally proposed by Kołodziej et al. [43], who considered the elasto-plastic properties of prismatic bars using the MFS. The use of Picard iteration has
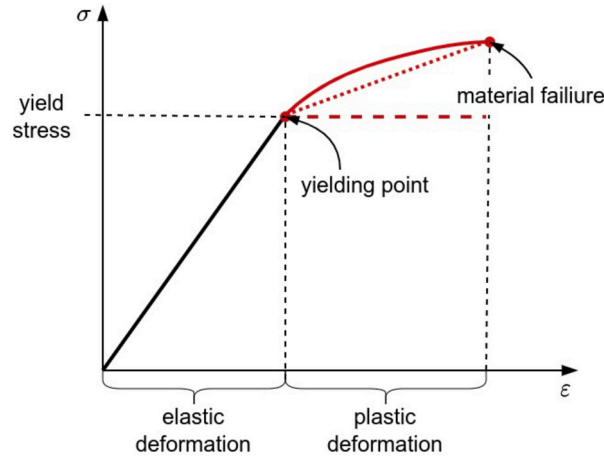
Fig. 1. Sketch of stress and strain relation as a result of a uniaxial tension test.

also been recently reported in the elasto-plastic torsion problem [44] using the MFS and in the Taylor series expansion with moving least squares [45].

The layout of the paper is as follows: In Section 2, we briefly revisit the theoretical background of elasto-plastic deformations, in Section 3, we provide a detailed description of the proposed solution procedure employing meshless methods – including domain discretization, approximation of the differential operators and discretization of the governing equations, in Section 4, analytic and FEM solutions are used to validate the proposed methodology on three different cases, in Section 5, we solve a two-dimensional problem on an irregular domain, while, in Section 6, our conclusions and findings are gathered.

2. Iterative algorithm for solving elasto-plastic deformation problems

Plastic deformation, also known as *plasticity*, is the phenomenon when the shape of a solid material undergoes irreversible changes in response to applied forces, i.e. the internal structure of the material is changed during the deformation. The transition from elastic to plastic behaviour is known as *yielding*, and the ability to predict this transition is important for the engineering of structures and components subjected to different loads and environmental conditions. Typically, uniaxial tensile tests are performed to gain insight into the response characteristics of a material when subjected to external loads. When such tests are performed on a ductile material, the result is a *stress-strain* relationship curve as conceptually illustrated in Fig. 1.

In the first segment, the material undergoes *elastic deformation*. Since the relationship between stress and strain in this segment is linear, it is often referred to as *linear elastic deformation*, where the slope of the curve is the elastic Young's modulus E. If the applied load is released before the *yield stress* is reached, the material returns to its original state without permanent structural changes. However, if the applied loads introduce internal stresses that exceed the yield stress, the total deformation observed becomes a sum of two contributions — the plastic and the elastic part.

The relationship between stress and strain beyond the *yielding point* is commonly referred to as the *hardening curve*. If the material under consideration is unloaded in this segment, the object no longer returns to its original shape. Instead, at least parts of it remain *plastically deformed*. Different materials exhibit different hardening curves, which are marked in red in Fig. 1. A frequently considered simplification of the hardening curve is *ideal plasticity*, in which the yield stress is constant beyond the yielding point (see dashed red line in Fig. 1). Another common modelling approach is to use the linear hardening curve, which is marked with the red dotted line. Such a modelling approach leads to a *bilinear* elastic-plastic material behaviour, since both the elastic and the plastic regimes are governed by a linear stress-strain relation. In this case, the Young's modulus E denotes the slope in the elastic regime and the hardening rate H denotes the slope in the plastic regime. In practice, the hardening regime is usually represented as a curve that is fitted to experimental data obtained from uniaxial tensile tests, whereby in the simplest case a piecewise linear fit is made between the experimental data points, which leads to *multilinear material models*.

The study presented in this work is limited to rate-independent materials, where the deformation of the material under consideration does not depend on the rate of applied loads. The study is also limited to *isotropic hardening*, where the evolution of the yield stress surface corresponds to a uniform (isotropic) expansion of the initial yield surface. A detailed discussion of other stress-strain relationships and different types of hardening can be found in [11].

Initially, the deformation is elastic, as depicted in Fig. 1. The principal assumption of linear elasticity is that, when subjected to external forces, a body deforms linearly – obeying Hooke's law. Thus, the stress tensor $\boldsymbol{\sigma}$ is defined as the product of the elasticity tensor D^e and the strain tensor $\boldsymbol{\varepsilon}$,

$$\boldsymbol{\sigma} = D^e \boldsymbol{\varepsilon}, \tag{1}$$

commonly expressed as $D^e = 2\mu I_S + \lambda \mathbf{I} \otimes \mathbf{I}$, for symmetric identity tensor I_S, identity matrix $\mathbf{I}$ and first and second Lamé parameters λ and μ, respectively. Lamé parameters are commonly expressed in terms of Young's modulus E, and Poisson's ratio ν as

$$\lambda = \frac{E\nu}{(1-2\nu)(1+\nu)} \quad \text{and} \quad \mu = \frac{e}{2(1+\nu)}. \tag{2}$$

Under small-strain assumption the strain tensor ϵ and displacement vector $\vec{u}$ are related as

$$\epsilon = \frac{\nabla\vec{u} + (\nabla\vec{u})^\mathsf{T}}{2}. \tag{3}$$

Considering (1) and (3) and the stationary Cauchy momentum equation in the absence of external forces ($\nabla \cdot \sigma = 0$), one gets a well-known Navier-Cauchy equation

$$(\lambda + \mu)\nabla(\nabla \cdot \vec{u}) + \mu\nabla^2\vec{u} = 0, \tag{4}$$

describing the linear-elastic deformation.

Two main types of boundary conditions are often used: essential boundary conditions and traction boundary conditions, also known as natural boundary conditions. Essential boundary conditions are used to define displacements $\vec{u}_0$ along certain parts of the domain boundary, denoted by $\vec{u} = \vec{u}_0$. On the other hand, the traction boundary conditions are concerned with defining the surface traction $\vec{t}_0$, expressed as $\sigma\vec{n} = \vec{t}_0$, where $\vec{n}$ is the outward-facing unit normal to the boundary of the domain.

Upon surpassing a critical stress threshold (*yield stress* σ_y), the material undergoes localised irreversible plastic deformation. In the plastic regime, the total local deformation has two contributions. One due to the elastic strain ϵ^e and another due to the plastic strain ϵ^p. The sum of both is referred to as the total strain $\epsilon = \epsilon^e + \epsilon^p$. In the plastic regime, the Navier-Cauchy (4) is therefore no longer valid. To check its validity, different criteria such as the Tresca, the Mohr-Coulomb, the von Mises yield or the Drucker-Prager criterion [11] can be used. In this paper we focus on the von Mises yield criterion, which assumes that the yield stress (σ_y) is a function of the scalar equivalent plastic strain $\overline{\epsilon}^p$ (see Fig. 15 as an example of such a stress-strain relationship). The criterion is based on the yield function Φ, which is defined as

$$\Phi = \sigma_{\mathrm{VMS}n} - \sigma_y(\overline{\epsilon}^p_n), \tag{5}$$

where a scalar value $\overline{\epsilon}^p$ denotes the accumulated plastic strain and σ_{VMS} stand for von Mises stress defined as

$$\sigma_{\mathrm{VMS}} = \frac{1}{\sqrt{2}}\left[(\sigma_{xx}-\sigma_{yy})^2 + (\sigma_{yy}-\sigma_{zz})^2 + (\sigma_{zz}-\sigma_{xx})^2(\sigma_{xx}-\sigma_{yy})^2 + 6\left(\sigma_{xy}^2 + \sigma_{yz}^2 + \sigma_{xz}^2\right)\right]^{\frac{1}{2}}. \tag{6}$$

If $\Phi > 0$, the material locally undergoes plastic deformation, otherwise the deformation is elastic:

$$\begin{cases} \Phi \le 0, & \text{elastic deformation} \rightarrow \text{solution of Navier-Cauchy locally } \textbf{valid} \\ \Phi > 0, & \text{plastic deformation} \rightarrow \text{solution of Navier-Cauchy is locally } \textbf{invalid}. \end{cases} \tag{7}$$

In the elastic regime, the Navier-Cauchy solution is accepted, while in the plastic regime a correction is applied that adjusts the calculated stresses and strains and account for plastic effects.

Since the stress state reflects the history of the applied stress, the problem can be solved incrementally by applying partial loads to the body that eventually add up to the total load [11,46]. The key concept behind this approach is that each partial load applied to the body is assumed to result in a purely elastic deformation. Thus, an initial estimate is obtained by solving the Navier-Cauchy Equation (4), which leads to a vector field of displacement increments $\delta\vec{u}$ corresponding to the amount of the applied partial load. In the i-th load step, $i \le N_{\mathrm{load}}$, the following set of bulk state predictions is obtained

$$\begin{aligned} \vec{u}_i &= \vec{u}_{i-1} + \delta\vec{u}, \\ \delta\epsilon &= \frac{\nabla(\delta\vec{u}) + (\nabla(\delta\vec{u}))^\mathsf{T}}{2}, \\ \epsilon_i^e &= \epsilon_{i-1}^e + \delta\epsilon, \\ \epsilon_i^p &= \epsilon_{i-1}^p, \\ \overline{\epsilon}_i^p &= \overline{\epsilon}_{i-1}^p, \\ \sigma_i &= \mathrm{D}^e\epsilon_i^e, \end{aligned} \tag{8}$$

and the stress tensor is calculated only from the elastic strain.

In the next step, we check the validity of the stress by evaluating the yield criterion (7). If $\Phi \le 0$, the yield condition has not been violated and the assumed elastic deformation calculated with (4) is valid. If $\Phi > 0$, however, the prediction of purely elastic deformation was wrong. Therefore, the solution must first be adapted locally according to the *return mapping procedure*. We use the single-equation return mapping scheme as proposed in [11]. For this purpose, an incremental plastic multiplier $\Delta\gamma$ is introduced.

The aim of the return mapping procedure is to find such a $\Delta\gamma$ that fulfils the following equality [11]

$$\Phi = \sigma_{\mathrm{VMS}i} - 3\mu\Delta\gamma - \sigma_y(\overline{\epsilon}_i^p + \Delta\gamma) = 0. \tag{9}$$

We use a Newton-Raphson approach (see Algorithm 1 for details) to solve (9) and finally, with the computed $\Delta\gamma$, the local bulk state variables are temporarily updated

$$\mathbf{s}_i^{j+1} = \left(1 - \frac{\Delta\gamma 3\mu}{\sigma_{\mathrm{VMS}\,i}^{\,j}}\right)\mathbf{s}_i^{\,j},$$

$$\boldsymbol{\sigma}_i^{j+1} = \mathbf{s}_{i+1}^{j+1} + p_{i+1}^{j+1}\mathbf{I},$$

$$\boldsymbol{\varepsilon}_i^{\mathrm{e}\,j+1} = \frac{1}{2\mu}\mathbf{s}_{i+1}^{j+1} + \frac{1}{3}\varepsilon_{v\,i}^{\mathrm{e}\,j}\mathbf{I}, \tag{10}$$

$$\overline{\varepsilon}_i^{p\,j+1} = \overline{\varepsilon}_i^{p\,j} + \Delta\gamma,$$

where $\mathbf{s}$ and p denote the deviatoric and hydrostatic components of the stress tensor and $\varepsilon_v^{\mathrm{e}} = \sum \mathrm{diag}(\boldsymbol{\varepsilon}^{\mathrm{e}})$ is the volumetric component of the elastic strain and j denotes the global optimisation index. The updated stress $\boldsymbol{\sigma}_i^{j+1}$ does not fulfill Navier-Cauchy equation anymore, i.e.

$$\nabla \cdot \boldsymbol{\sigma}_i^{j+1} = -\delta\vec{r}, \tag{11}$$

where vector $\vec{r} \neq 0$ stands for residual. To drive the state towards correct solution a global optimisation is performed. In our case we use the Picard iteration to perform the global optimization, where (11) is set as the RHS of (4), and the whole process repeats until

$$\left\|\delta\vec{r}\right\| < \epsilon_{\mathrm{tol}} \tag{12}$$

holds in all of the nodes with ϵ_{tol} standing for prescribed tolerance [46]. Note, that during global optimization, the boundary conditions need to be updated accordingly, e.g., at the i-th load step, the total prescribed stress at the boundary Ω is

$$\boldsymbol{\sigma}(\Omega) = \boldsymbol{\sigma}_{\mathrm{load}\,i} = \sum_i \delta\boldsymbol{\sigma}, \tag{13}$$

and after j global optimization steps, this boundary condition reads

$$\boldsymbol{\sigma}(\Omega) = \boldsymbol{\sigma}_{\mathrm{load}\,i} - \boldsymbol{\sigma}(\Omega)_i^j. \tag{14}$$

Once the current load step converges, a new partial load is applied, and the whole process is repeated until the sum of partial loads equals the prescribed total load.

Algorithm 1 Return mapping algorithm.

Input: Material properties Π, maximum return mapping iterations $I_{\max}$ and return mapping tolerance ϵ_{tol}.
Output: Incremental plastic multiplier $\Delta\gamma$.

1: **function** RETURN_MAPPING($\Pi, I_{\max}, \epsilon_{\mathrm{tol}}$)
2:     $k \leftarrow 0$ ▷ Initializing iteration counter.
3:     $\Phi^\star \leftarrow \sigma_{\mathrm{VMS}\,n} - \sigma_y(\overline{\varepsilon}_n^p)$ ▷ Initializing residual yield function value.

4:     // Newton-Raphson iteration:
5:     **do**
6:         $H \leftarrow \left.\frac{\mathrm{d}\sigma_y}{\mathrm{d}\overline{\varepsilon}^p}\right|_{\overline{\varepsilon}_n^p + \Delta\gamma}$ ▷ Hardening curve slope evaluated at $\overline{\varepsilon}_n^p + \Delta\gamma$.
7:         $\Delta\gamma \leftarrow \Delta\gamma + \frac{\Phi^\star}{3\mu + H}$ ▷ New guess for $\Delta\gamma$.
8:         $\Phi^\star = \sigma_{\mathrm{VMS}\,n} - 3\mu\Delta\gamma - \sigma_y(\overline{\varepsilon}_n^p + \Delta\gamma)$ ▷ Re-evaluate residual.
9:         $k = k + 1$ ▷ Increase number of Newton-Raphson iterations.
10:     **while** $|\Phi^\star| > \epsilon_{\mathrm{tol}}$ and $k < k_{\max}$

11:     **return** $\Delta\gamma$ ▷ Return incremental plastic multiplier $\Delta\gamma$.
12: **end function**

The backbone of the above solution procedure is the numerical treatment of the Navier-Cauchy (4) PDE that requires an appropriate domain discretisation, partial differential operators discretisation and ultimately solution of global sparse system resulting from the discretisation of the (4). All these steps are discussed in detail in the following section.

The entire solution procedure demonstrated in Algorithm 2 and schematically presented in Fig. 2.

3. Solution to Navier-Cauchy equation using RBF-FD approximation

In this section, we will discuss how to numerically solve the Navier-Cauchy equation (4) using the RBF approximation on scattered nodes. In the first step, the domain Ω and its boundary are populated with discrete nodes at which the solution is to be calculated. Afterwards, linear differential operators governing the equation at hand are approximated at each node $\mathbf{x}_i \in \Omega$. In the third step, the Navier-Cauchy equation is approximated by a system of algebraic equations, which is represented as a global sparse system. In the last step, the sparse system is solved, which leads to a numerical solution. In the following subsections, each of the above steps is discussed.

Algorithm 2 Solution procedure algorithm.

Input: The problem, nodal density function h, stencil size n, linear differential operators $\mathcal{L}$, approximation basis ξ, material properties Π, number of load steps N_{load}, external load σ_{load}, maximum return mapping iterations I_{max} and return mapping tolerance ϵ_{tol}.

Output: Deformation field **u** and corresponding stress and strain tensors σ and ε respectively.

1: **function** SOLVE(problem, $h, n, \xi, \Pi, N_{\text{load}}, \sigma_{\text{load}}, I_{\text{max}}, \epsilon_{\text{tol}}$)
2:     $\Omega \leftarrow$ DISCRETISE_DOMAIN(h)   ▷ Discretize the domain.
3:     $\mathcal{L} \leftarrow$ APROXIMATE(problem, ξ, Ω, n)   ▷ Differential operator approximation.
4:     **for** $i \leftarrow 0$ **to** N_{load} **do**
5:         $\delta \vec{u} = \mathbf{0}$ ▷ Initalize displacement changes.
6:         $\delta \vec{r} = \mathbf{0}$ ▷ Initalize residuum force changes.
7:
8:         // Picard iteration
9:         **do**
10:             $\delta \vec{u} \leftarrow$ SOLVE_ELASTIC(problem, $\Pi, \delta \vec{r}, \partial \sigma_{\text{load}}$)   ▷ Linear-elastic guess for partial load $\partial \sigma_{\text{load}} = \frac{\sigma_{\text{load}}}{N_{\text{load}}}$.
11:             $\vec{u} = \vec{u} + \delta \vec{u}$
12:             $\varepsilon, \sigma \leftarrow$ PROCESS($\vec{u}, \Pi$)   ▷ Compute strain and stress tensors.
13:
14:             **for each** $\vec{p}$ **in** Ω **do**
15:                 **if** $\sigma_{\text{VMS}}(\vec{p}) > \sigma_{\text{yield}}$ **then**
16:                     $\sigma(\vec{p}), \varepsilon(\vec{p}) \leftarrow$ RETURN_MAPPING($I_{\text{max}}, \epsilon_{\text{tol}}, \Pi$)
17:                 **end if**
18:             **end for**
19:             $\delta \vec{r} \leftarrow$ COMPUTE_RESIDUUM(σ)   ▷ Estimate residuum forces.
20:         **while** MAX($\|\delta \vec{r}\|$) > ϵ_{tol} ▷ Repeat until residuum forces are sufficiently small.
21:     **end for**
22:     **return** $\varepsilon, \sigma, \vec{u}$ ▷ Return strains, stresses and displacements for all computational nodes.
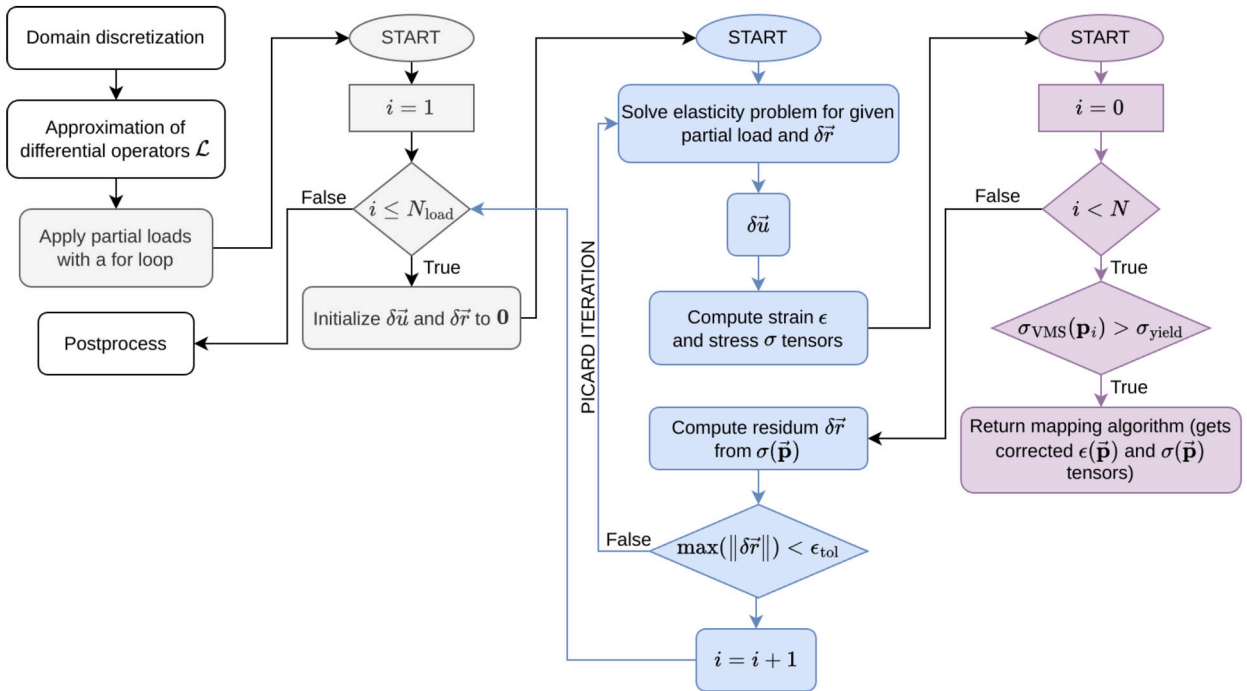23: **end function**

Fig. 2. Schematic presentation of Algorithm 2. Note that elements of each loop are marked with different colour.

3.1. Node generation

In the RBF community, an established approach for stable and accurate RBF approximation is to discretise domain of interest with quasi-uniformly scattered nodes [47,17]. Although there is still no generally accepted consensus on a measure of node quality, two quantities are often considered for this purpose, namely the minimum distance between any pair of nodes, often referred to as the separation distance, and the maximum empty space without nodes, commonly referred to as the fill distance. Here we use an algorithm that generates nodes according to the above guidelines [18] and has been used many times in RBF-related research [48,32,49–51].

The algorithm is of an iterative advancing-front type. It begins with start nodes that are placed in an *expansion queue*. In our particular case, we first distribute the nodes on the boundary, and since the boundary is one-dimensional, they can trivially be distributed

uniformly (Fig. 5, far left). In each iteration, a node is selected from a queue and expanded by generating new candidates (in our case 12 candidates) uniformly on a randomly rotated annulus around the processed point. Note that for different randomisations, i.e. different random *seeds*, of the annulus rotations, we obtain different node layouts, all conforming to the quasi-uniformity guidelines. These candidates are then processed, discarding those that are outside the domain or too close to existing nodes. In the final iteration step, the nodes that were not discarded are placed in a queue. The iteration is continued until the queue is empty to ensure that the domain is fully covered with nodes.

The algorithm is dimension-independent and capable of populating complex geometries. It also allows variable internodal distances, which can be used as cornerstones for h [31] or hp [32] adaptivities. It has also been further developed for the generation of nodes on parametric surfaces [19] as well as for domains whose boundaries are represented as CAD models [23], and tailored for parallel execution on shared memory architectures [52]. Interested readers are referred to the original paper [18] for more details on the node generation algorithm or its standalone C++ implementation in the *Medusa library* [53].

3.2. Approximation of differential operators

After computational nodes have been positioned, linear differential operators of the governing system of PDEs are approximated using a set of nearby nodes, commonly referred to as *stencil nodes*. While different stencil selection strategies have been proposed [54, 55], we resort to the most common approach using a cloud of closest n nodes.

Let us assume a linear differential operator $\mathcal{L}$ in point $\mathbf{x}_c \in \Omega$ and its stencil nodes $\{\mathbf{x}_c\}_{i=1}^n = \mathcal{N}$. The approximation is then sough using ansatz

$$(\mathcal{L}g)(\vec{x}_c) \approx \sum_{i=1}^n w_i^{\mathcal{L}} g(\vec{x}_i), \tag{15}$$

for any function g and unknown weights $\mathbf{w}^{\mathcal{L}}$ that are obtained by enforcing the equality of approximation (15) for a chosen set of basis functions $\mathbf{f}(\vec{x})$, i.e.

$$\sum_{i=1}^n w_i f_j(\vec{x}_i) = (\mathcal{L}f_j)(\vec{x}_c). \tag{16}$$

Gathering all n equations for a given stencil results in a linear system

$$\mathbf{Fw} = \boldsymbol{\ell}_f, \qquad \mathbf{F} = \begin{bmatrix} f(\|\vec{x}_1 - \vec{x}_1\|) & \cdots & f(\|\vec{x}_n - \vec{x}_1\|) \\ \vdots & \ddots & \vdots \\ f(\|\vec{x}_1 - \vec{x}_n\|) & \cdots & f(\|\vec{x}_n - \vec{x}_n\|) \end{bmatrix}, \qquad \ell_f^i = \left(\mathcal{L}f_i(\vec{x}) \right)\Big|_{\vec{x}=\vec{x}_c}. \tag{17}$$

In this work, Polyharmonic Splines (PHS) are used as an approximation basis defined as

$$f(r) = \begin{cases} r^k, & k \text{ odd} \\ r^k \log r, & k \text{ even} \end{cases} \tag{18}$$

for Euclidean distance r. A particularly appealing property of PHS is the lack of shape parameter [56].

Note that it has previously been observed that the use of PHS as basis functions does not guarantee convergent behaviour or solvability [47]. Convergent behaviour and conditional positive definiteness can be guaranteed if the approximation basis is expanded with monomials [57,47,58]. Therefore, the system (17) is augmented with $N_p = \binom{m+d}{d}$ monomials p with orders up to (and including) degree m for a d-dimensional domain, which results in an overdetermined system of equations describing the constrained optimization problem [58]. In practice, the weights $\mathbf{w}$ are expressed as a solution to the equation

$$\begin{bmatrix} \mathbf{F} & \mathbf{P} \\ \mathbf{P}^\top & \mathbf{0} \end{bmatrix} \begin{bmatrix} \mathbf{w} \\ \lambda \end{bmatrix} = \begin{bmatrix} \boldsymbol{\ell}_f \\ \boldsymbol{\ell}_p \end{bmatrix}, \tag{19}$$

with the matrix $\mathbf{P}$ of the evaluated monomials and Lagrangian multipliers λ that are discarded once the weights are computed.

The discussed approach is also known as a RBF generated finite differences method (RBF-FD) that is a popular choice in the meshless community due to its stability [33,59]. For a stable RBF-FD approximation, the stencil size is chosen as

$$n = 2\binom{m+d}{d}, \tag{20}$$

for a d-dimensional domain as recommended in [29]. For clarity, example stencil sizes n for different orders of monomial augmentation m are shown in Table 1.

3.3. Navier-Cauchy equation discretization

In previous sections we discussed how to numerically approximate differential operators on scattered nodes, in this subsection, we discuss the discretisation of the Navier-Cauchy equation (4). Since we deal with a two dimensional domain, we first express the governing problem component-wise $\vec{u} = (u, v)$ as

Table 1
Example stencil sizes in different dimensions for various augmentation orders.

m	$d = 1$	$d = 2$	$d = 3$
2	6	12	20
4	10	30	70
6	14	56	168

$$(\lambda + \mu)\frac{\partial}{\partial x}\left(\frac{\partial u}{\partial x} + \frac{\partial v}{\partial y}\right) + \mu\left(\frac{\partial^2 u}{\partial x^2} + \frac{\partial^2 u}{\partial y^2}\right) = 0 \quad \text{and} \tag{21}$$

$$(\lambda + \mu)\frac{\partial}{\partial y}\left(\frac{\partial u}{\partial x} + \frac{\partial v}{\partial y}\right) + \mu\left(\frac{\partial^2 v}{\partial x^2} + \frac{\partial^2 v}{\partial y^2}\right) = 0, \tag{22}$$

and natural boundary conditions

$$t_{0x} = \mu n_y \frac{\partial u}{\partial y} + \lambda n_x \frac{\partial v}{\partial y} + (2\mu + \lambda)n_x\frac{\partial u}{\partial x} + \mu n_y\frac{\partial v}{\partial x} \quad \text{and} \tag{23}$$

$$t_{0y} = \mu n_x \frac{\partial u}{\partial y} + (2\mu + \lambda)n_y\frac{\partial v}{\partial y} + \lambda n_2\frac{\partial u}{\partial x} + \mu n_x\frac{\partial v}{\partial x}, \tag{24}$$

with surface traction $\vec{t_0} = (t_{0x}, t_{0x})$ and outward-facing unit normal to the domain boundary $\vec{n} = (n_x, n_y)$.

The aim here is to transform the above PDEs into a system of algebraic equations. To do so, equations (22) and (24) are considered in N computational nodes, where corresponding partial differential operators are discretised using (15), resulting in a global system schematically represented as [60]

$$\begin{bmatrix} \mathbf{W}_{11} & \mathbf{W}_{12} \\ \mathbf{W}_{21} & \mathbf{W}_{22} \end{bmatrix} \begin{bmatrix} \mathbf{u} \\ \mathbf{v} \end{bmatrix} = \begin{bmatrix} \mathbf{b}_1 \\ \mathbf{b}_2 \end{bmatrix}, \tag{25}$$

where $\mathbf{u}$ and $\mathbf{v}$ stand for vector of size N containing the unknown discrete displacements components. Vectors $\boldsymbol{b_1}$ and $\boldsymbol{b_2}$ hold RHS and boundary conditions values and in blocks $\mathbf{W}_{11}, \mathbf{W}_{12}, \mathbf{W}_{21}, \mathbf{W}_{22}$ stencil weights (19) are stored. To discretise the Navier-Cauchy equation, stencil weights for approximation of first and second derivatives $\mathbf{w}_i^{\partial x}, \mathbf{w}_i^{\partial y}, \mathbf{w}_i^{\partial^2 x}, \mathbf{w}_i^{\partial^2 y}, \mathbf{w}_i^{\partial xy}$ are required in each node i (how to compute those is discussed in section 3.2). To assemble the system (25), we also need a vector of stencil nodes of i-th discretisation node $\mathcal{N}(i)$. The system is finally expressed as

$$\left.\begin{aligned} W_{11}^{i,\mathcal{N}(i)_j} &= \left[(\lambda + 2\mu)\mathbf{w}_i^{\partial^2} + \mu\mathbf{w}_i^{\partial^2 y}\right]_j \\ W_{12}^{i,\mathcal{N}(i)_j} &= \left[(\lambda + \mu)\mathbf{w}_i^{\partial x\partial y}\right]_j \\ \boldsymbol{b}_{1i} &= 0 \end{aligned}\right\}, \tag{26}$$

$$\left.\begin{aligned} W_{21}^{i,\mathcal{N}(i)_j} &= \left[(\lambda + \mu)\mathbf{w}_i^{\partial x\partial y}\right]_j \\ W_{22}^{i,\mathcal{N}(i)_j} &= \left[\mu\mathbf{w}_i^{\partial^2 x} + (\lambda + 2\mu)\boldsymbol{\chi}_i^{\partial^2 y}\right]_j \\ \boldsymbol{b}_{2i} &= 0 \end{aligned}\right\}, \tag{27}$$

with $i \in [1, N]$ and $j \in [1, n]$. In the same manner the lines representing the normal boundary conditions are assembled

$$\left.\begin{aligned} W_{11}^{i,\mathcal{N}(i)_j} &= \left[\mu n_2\mathbf{w}_i^{\partial y} + (2\mu + \lambda)n_1\mathbf{w}_i^{\partial x}\right]_j \\ W_{12}^{i,\mathcal{N}(i)_j} &= \left[\lambda n_1\mathbf{w}_i^{\partial y} + \mu n_2\mathbf{w}_i^{\partial x}\right]_j \\ \boldsymbol{b}_{1i} &= t_{0x,1} \end{aligned}\right\}, \tag{28}$$

$$\left.\begin{aligned} W_{21}^{i,\mathcal{N}(i)_j} &= \left[\mu n_1\mathbf{w}_i^{\partial y} + \lambda n_2\mathbf{w}_i^{\partial x}\right]_j \\ W_{22}^{i,\mathcal{N}(i)_j} &= \left[\mu n_1\mathbf{w}_i^{\partial x} + (2\mu + \lambda)n_2\mathbf{w}_i^{\partial y}\right]_j \\ \boldsymbol{b}_{2i} &= t_{0y,i} \end{aligned}\right\}, \tag{29}$$

while in essential boundary conditions nodes, we simply express

$$\begin{aligned} W_{11}^{i,i} &= 1 \\ \boldsymbol{b}_{1i} &= u_{0x,i} \end{aligned} \quad \text{and} \quad \begin{aligned} W_{22}^{i,i} &= 1 \\ \boldsymbol{b}_{2i} &= u_{0y,i} \end{aligned} \quad . \tag{30}$$
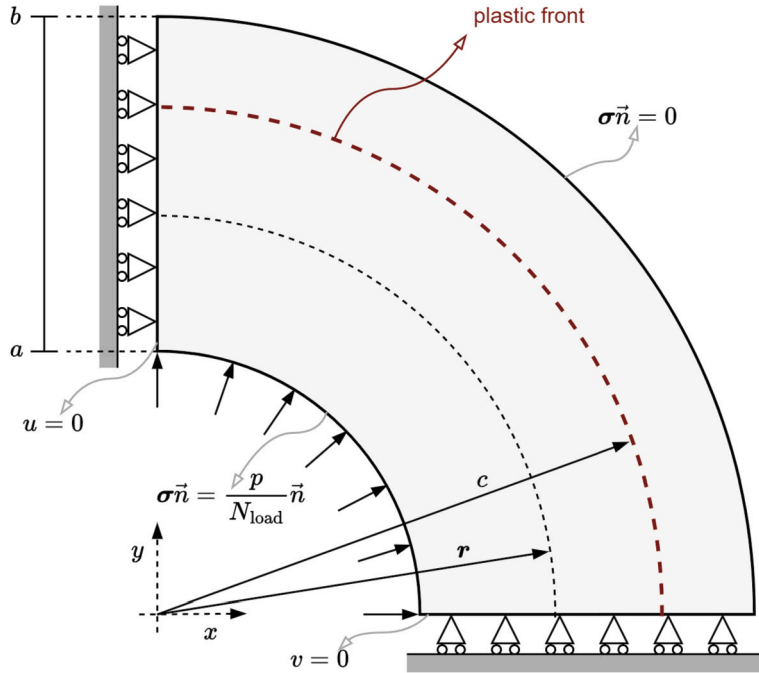
Fig. 3. Schematic representation of a pressurized thick-walled pipe expansion.

The example of assembled system is depicted in Fig. 6. Solving this system provides the numerical solution to the Navier-Cauchy problem as formulated in Equation (4).

3.4. Note on implementation and used parameters

The entire solution procedure is implemented in C++[1] and it is strongly dependent on our in-house open-source mesh-free project *Medusa* [53]. In all following analyses, a RBF-FD approximation with PHS basis of order $k = 3$ and augmenting monomials of order $m = 3$ on stencil size of $n = 20$ is used. The Picard iteration tolerance is set to $\epsilon_{\text{tol}} = 10^{-6}$. The final sparse linear system, is solved with the direct SparseLU using Eigen C++ library [61]. Post-processing was done with Python 3.10.6 and Jupyter notebooks, also available in the provided git repository.[1]

The code[1] was compiled using `g++ (GCC) 11.3.0` for Linux with `-O3 -DNDEBUG` flags on `AMD EPYC 7713P 64-Core Processor` computer. The highest RAM usage during the computation was approximately 4 GB, thus, no RAM-related issues were encountered due to using the direct SparseLU solver in the process.

4. Numerical examples

The proposed solution procedure is applied to three different cases:

  (i) the linear-elastic case in Section 4.1,
 (ii) the perfectly plastic elasto-plastic case in Section 4.2 and
(iii) the elasto-plastic case with linear isotropic hardening in Section 4.3.

The first two problems have been extensively studied by other researchers. De Souza et al. [11] used FEM to obtain numerical solutions, while Hill [2] derived the analytical solutions. Here, both analytical and FEM solutions are used to evaluate the accuracy of the present solution procedure and to validate it.

The calculation domain is the same for all three cases: a thick-walled pipe with inner and outer radii $a = 100$ mm and $b = 200$ mm respectively. As shown schematically in Fig. 3, only a quarter of the pipe from the first quadrant is considered. The material properties were constant for all cases considered: Young's modulus $E = 210$ GPa, Poisson's ratio $\nu = 0.3$ and yield stress $\sigma_y = 0.24$ GPa. The left side of the pipe is constrained to move freely in the (vertical) y-direction, while the lower side of the pipe can only move in the (horizontal) x-direction. The outer wall of the pipe is traction free ($\boldsymbol{\sigma}\vec{\mathbf{n}} = 0$), while the inner wall is subjected to an internal pressure

---

[1] Source code is available at https://gitlab.com/e62Lab/public/p_2d_plasticity under tag *v1.0*.
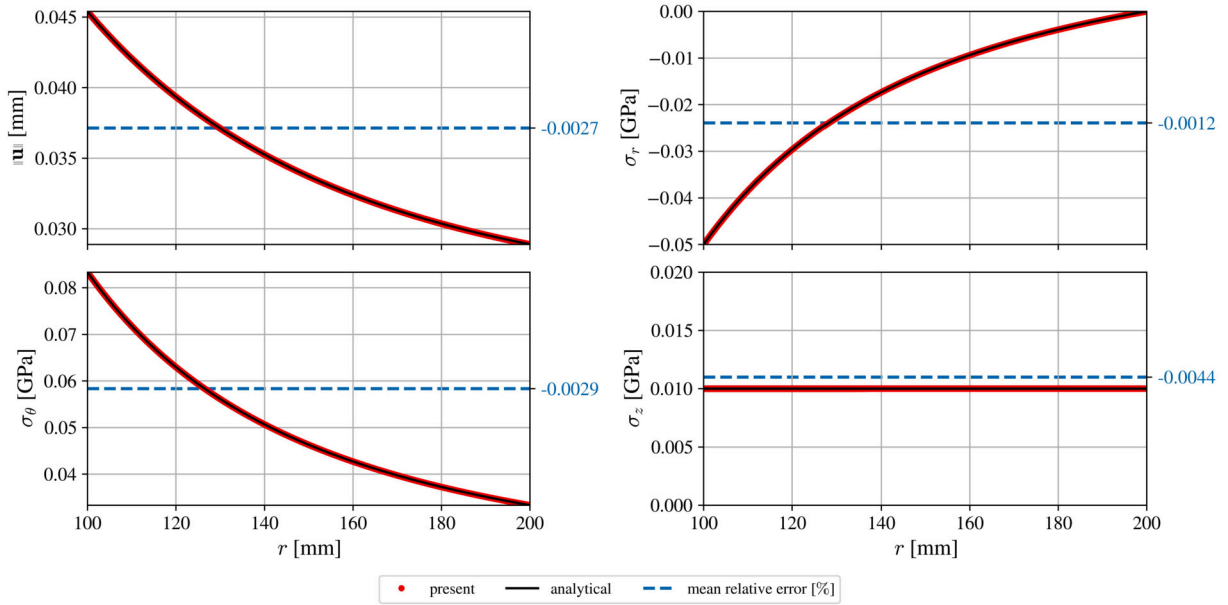
Fig. 4. Assessment of the present solution of the purely elastic case. The scattered plot is displaying the relative error in all nodes.

p, which, as explained in Section 2, is gradually increased until the full amount acts on the inner surface of the pipe, i.e. p/N_{load} is applied at each load step. All boundary conditions can also be found on the problem scheme in Fig. 3.

The amount of the internal pressure depends on the case considered: $0.05\,\text{GPa}$ for the linear elastic case, $0.19\,\text{GPa}$ for the perfectly plastic case and $0.175\,\text{GPa}$ for the case with linear isotropic hardening. Note that all the following analyses are performed assuming plane strain conditions, which means that the out-of-plane or z-direction strains are all zero, i.e. $\varepsilon_{zz} = \varepsilon_{xz} = \varepsilon_{yz} = 0$, and is thus applicable to the cross-sections of very thick (semi-infinite) bodies.

4.1. The linear elastic case

To establish the basic confidence level in the proposed solution procedure, the internal pressure p is set to a value of $0.05\,\text{GPa}$, which is intentionally low, to assure that all deformations are well within the elastic regime. The case has an analytic solution [11,2] given in cylindrical coordinates

$$
\sigma_r = -\left(\frac{\frac{b^2}{r^2} - 1}{\frac{b^2}{a^2} - 1}\right) p, \qquad \sigma_z = \frac{2\nu}{\frac{b^2}{a^2} - 1} p,
$$

$$
\sigma_\theta = \left(\frac{\frac{b^2}{r^2} + 1}{\frac{b^2}{a^2} - 1}\right) p, \qquad u_r = \frac{p}{e} \frac{(1+\nu)(1-2\nu)r + (1+\nu)\frac{b^2}{r}}{\frac{b^2}{a^2} - 1}, \tag{31}
$$

which we use for verification of the Navier-Cauchy solver.

To verify the performance of the proposed solution procedure using scattered nodes, we numerically solve the problem in Cartesian coordinate system. In Fig. 4, the RBF-FD solution is compared with the (31). We see that the present method agrees well with the closed-form solution, with the relative error of the numerical solution being well below $1\%_0$ when $N \approx 95\,000$ nodes are used. In the right plot of Fig. 5, we vary the internodal distance h and examine its effect on the accuracy of the numerical solution when the local field description improves. The error $\left\| \mathbf{u}(\mathbf{x}_i) - u_r(\mathbf{x}_i)\mathbf{e}_r(\mathbf{x}_i) \right\|$ is calculated for each computational point $\mathbf{x}_i \in \Omega$ and the ℓ^2-norm of the numerical solution error is plotted against the number of discretization nodes N. For clarity, an example of the spatial distribution of the error of the displacement magnitude is shown in the centre of Fig. 5. Since there is practically an infinite number of possible node layouts for a given h, which depend on the number and position of the seed nodes, the number of expansion candidates and different randomisations (random *seed*) during candidate generation, we also test the spread of the solutions with respect to this variation. The left graph in Fig. 5 shows two different node layouts with different settings for the initial node generation. For each data point in the right plot of Fig. 5, we varied the node generation setting and obtained an ensemble of 10 solutions as a result. The ensemble converges in both respects, i.e. the finer the domain discretizations the higher the accuracy and the lower the scatter.

Note that all solutions in this section were obtained by immediately forcing the full amount of internal pressure p, omitting the gradual load increase over N_{load} load steps for computation by setting $N_{\text{load}} = 1$. This is justified as only elastic deformations are expected and the solution procedure never encountered a local violation of the von Mises yield criterion from Equation (5), i.e. the return mapping Algorithm 1 was never used.
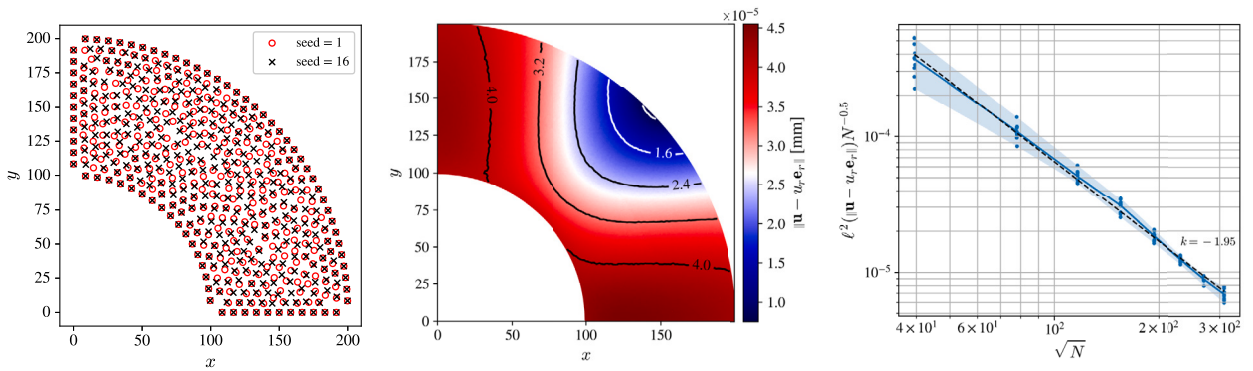
Fig. 5. An example of scattered nodes using two different random seeds (left), spatial distribution of the displacement magnitude error (middle) and convergence of the ℓ^2-norm of the displacement vector for the linear-elastic case (right).
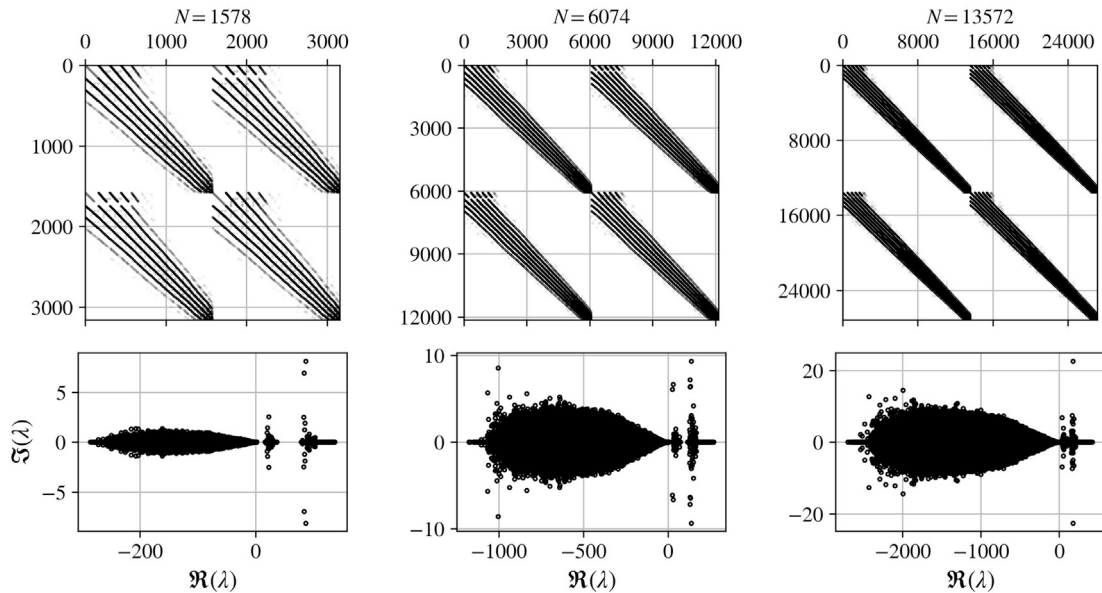

Fig. 6. Sparsity of final matrices (top row) and spectrum (bottom row) for three different discretization qualities.

The sparsity patterns of the final large sparse systems are shown in Fig. 6. The top row shows the sparsity of the systems for three different discretization qualities of the domain. The bottom row of Fig. 6 shows the spectra of the three matrices. The ratios between the real and imaginary parts of the eigenvalues agree well with previous studies [48,29,56]. Most eigenvalues have an order of magnitude larger real part compared to the relatively small imaginary parts.

4.2. Perfectly-plastic yielding of an internally pressurized thick-walled cylinder

With the established confidence in the implementation of the elastic deformation, the internal pressure p is increased to $0.19\,\mathrm{GPa}$, which is sufficient to initiate irreversible plastic deformations. The pressure p is gradually increased until a prescribed load is reached, as proposed in Algorithm 2.

For the cylindrically symmetric problem at hand, the plastic yielding starts at the inner surface ($r = a$) and gradually develops towards the outer surface ($r = b$) in the form of a circular front at $r = c$. The material collapses when the plastic front reaches the outer surface ($c = b$). At this point, the entire domain is plastically deformed and the external load required to reach this state is referred to as the *limit load*.[2]

Analytical solutions for the components of the normal stress tensor and for the radial displacement are given in [2,1]. Hill assumes the Tresca yielding criterion in his derivation, but argues that this can be a good approximation to the von Mises yielding

---

[2] For the present dimensions and material properties, the limit load is $p_{\mathrm{lim}} \approx 0.19209\,\mathrm{GPa}$ as discussed by de Souza [11].

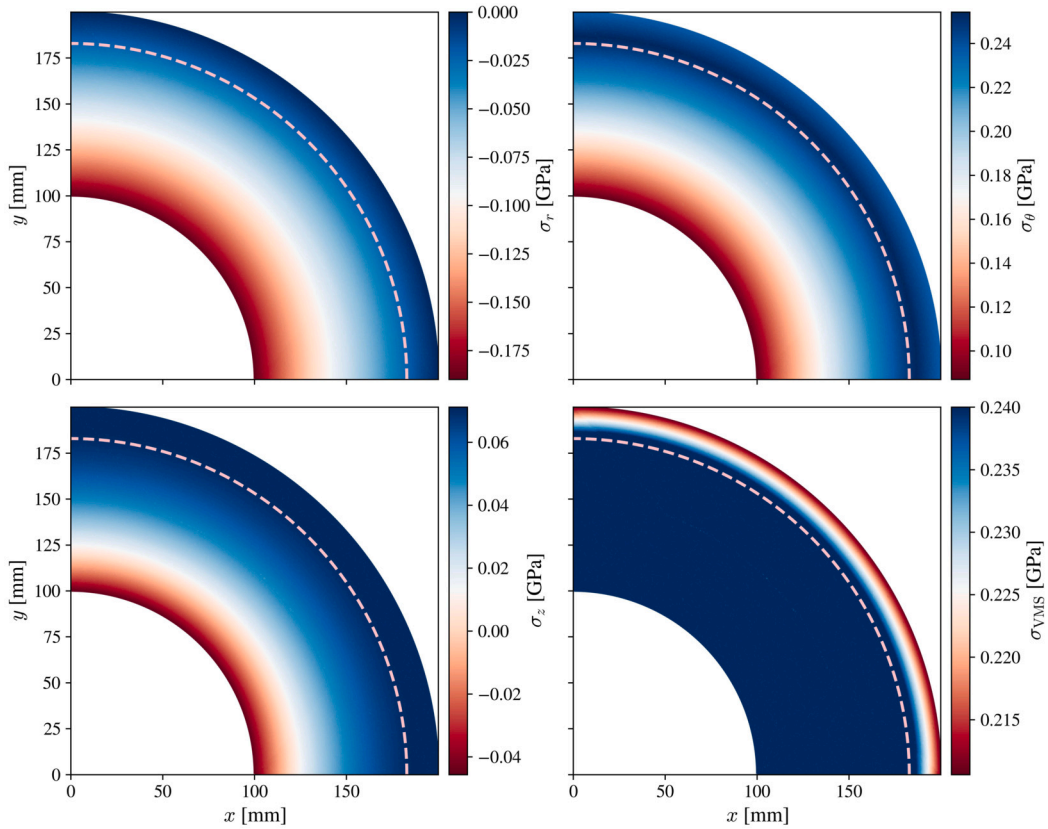**Fig. 7.** Example of numerical solution for perfectly plastic case at $p = 0.19\,\text{GPa}$, $N = 95\,300$ nodes at the final load step $N_{\text{load}} = 25$. The dashed line represents plastic front position $c = 186.67$ mm.

criterion [2]. Provided that the cylinder has started yielding, and the position of the plastic front within the cylinder is at c, the analytical approximations are as follows

$$
\left.
\begin{aligned}
\sigma_r &= -\frac{2c^2}{\sqrt{3}b^2}\left(\frac{b^2}{r^2} - 1\right)\sigma_y \\[2mm]
\sigma_\theta &= \frac{2c^2}{\sqrt{3}b^2}\left(\frac{b^2}{r^2} + 1\right)\sigma_y \\[2mm]
\sigma_z &= \frac{4vc^2}{\sqrt{3}b^2}\sigma_y
\end{aligned}
\right\} c \le r \le b,
\qquad
\left.
\begin{aligned}
\sigma_r &= -\frac{2}{\sqrt{3}}\left(1 - \frac{c^2}{b^2} + \ln\frac{c^2}{r^2}\right)\sigma_y \\[2mm]
\sigma_\theta &= \frac{2}{\sqrt{3}}\left(1 + \frac{c^2}{b^2} + \ln\frac{c^2}{r^2}\right)\sigma_y \\[2mm]
\sigma_z &= \frac{4vc^2}{\sqrt{3}}\left(\frac{c^2}{b^2} - \ln\frac{c^2}{r^2}\right)\sigma_y
\end{aligned}
\right\} a \le r \le c,
$$

$$
u_r = (1 - v)\frac{2\sigma_y c^2}{\sqrt{3}\mu r} + (1 - 2v)\frac{\sigma_r r}{2\mu}, \quad a \le r \le b,
\tag{32}
$$

where c is determined from its relation to the cylinder's internal pressure p as

$$
p = \frac{2\sigma_y}{\sqrt{3}}\left(1 - \frac{c^2}{b^2} + \ln\frac{c^2}{a^2}\right).
\tag{33}
$$

As in the previous case, we use Cartesian coordinates, even though the solution is given in cylindrical coordinates. In this case, the internal pressure has been gradually increased over $N_{\text{load}} = 25$ load steps. Example solution for the last load step corresponding to internal pressure $p = 0.19\,\text{GPa}$ is shown in Fig. 7. Figure shows the normal stresses σ_r, σ_θ and σ_z and the von Mises stress σ_{VMS}. Additionally, the plastic front at $c = 186.67$ mm is shown with a dashed pink line.

The accuracy of the numerical solution is further evaluated in Figs. 8 and 9, where the present solution procedure is compared with the analytical solution (see Equations (32)) and with the FEM solution. The commercial software package Abaqus was used to obtain the FEM solution. The FEM domain was discretized with a structured mesh consisting of 23 600 biquadratic plane strain quadrilaterals with 8 nodes (CPE8) with 71 473 nodes, which corresponds to a side length of the elements of approximately 1 mm.
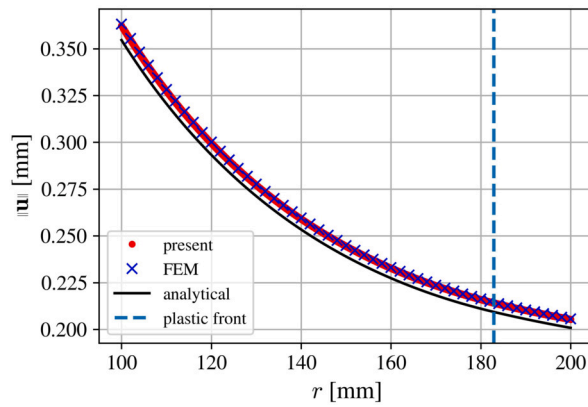
Fig. 8. Displacement magnitude $\|\mathbf{u}\|$ for the perfectly plastic case. For clarity, only every second point is shown for the FEM solution.
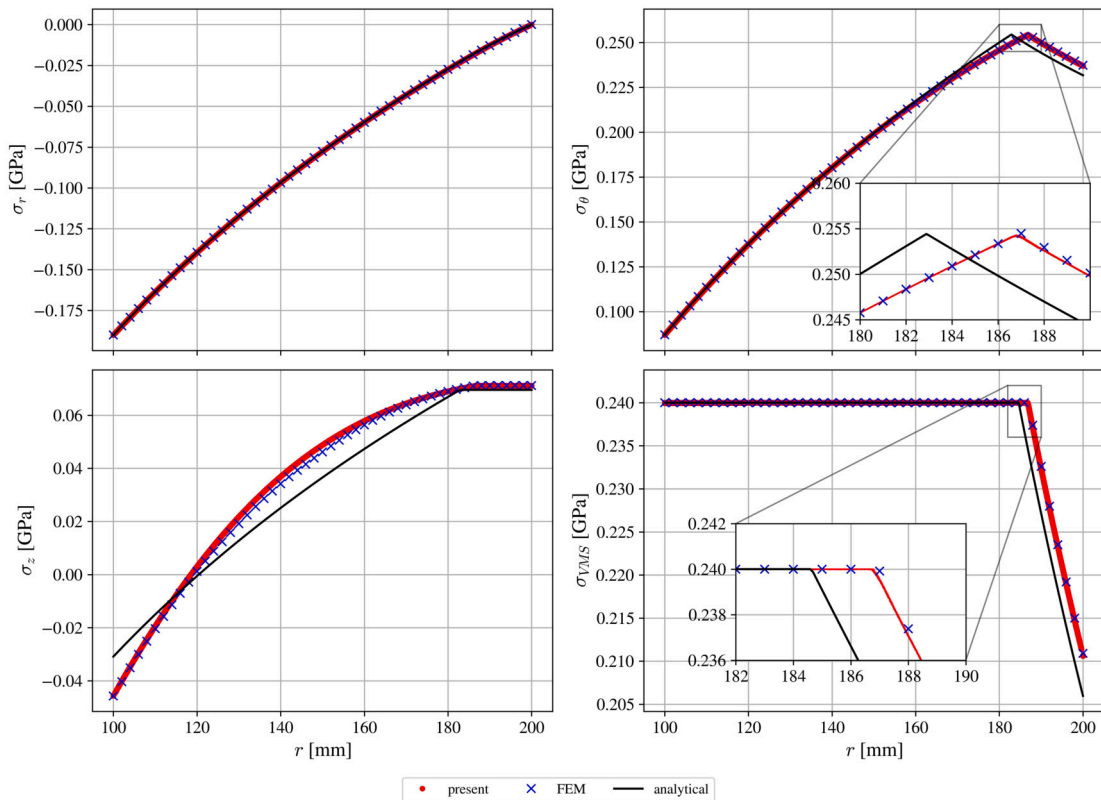

Fig. 9. Stress analysis in case of perfectly elasto-plastic problem.

Fig. 8 shows the displacement magnitude with respect to the radial coordinate r for all $N = 95\,300$ nodes of the present method and for nodes along the $y = 0$ line for the FEM approximation. We are pleased to observe that the proposed solution procedure shows good agreement with the FEM solution over the entire domain. However, both the FEM and the RBF-FD solution deviate slightly from the analytical solution. The most likely reason for the deviation from the analytical solution is the different yield criteria used.

In addition, Fig. 9 evaluates the performance of the present method in terms of stresses. In particular, the figure shows the normal stress components and the von Mises stress σ_{VMS} with respect to the radial coordinate r. There is a good agreement between the present method and the FEM solution, while both show some differences compared to the analytical solution, especially near the elastic-plastic interface.

4.2.1. The effect of load stepping

This section briefly discusses the influence of N_{load} on the solution accuracy and the convergence of the Picard iteration. In the left plot of Fig. 10, the effect of N_{load} on the final displacement accompanied with the average number of Picard iterations per step is
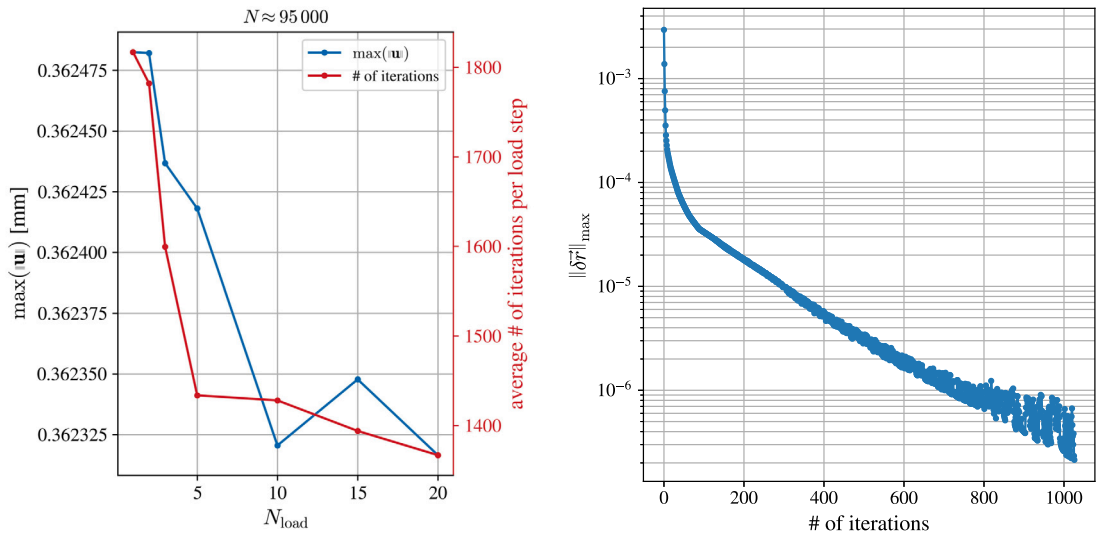
Fig. 10. The effect of number of load steps N_{load} on the accuracy of the numerical solution in terms of maximum displacement magnitude $\|\mathbf{u}\|$ and number of Picard iteration per step (left). Example of residual convergence at sixth load step in simulation with ten load steps (right).

Table 2
Constant values to reproduce the fit lines from Fig. 11.

regime	C_1	C_2	C_3	C_4
plastic	$-9.015 \cdot 10^1$	$2.751 \cdot 10^3$	$8.877 \cdot 10^{-2}$	1.123
elastic	$3.036 \cdot 10^2$	$-9.989 \cdot 10^3$	$-7.823 \cdot 10^{-1}$	-5.176

presented. We see that N_{load} has no effect on the final solution in this particular case, i.e. the maximum displacement is almost constant with respect to the N_{load} (note the scale of the left y-axis). On the other hand, increasing the N_{load} leads to additional computational effort. Although the average number of required Picard iterations per step decreases with increasing N_{load}, the cumulative number of iterations increases. The right-hand plot of Fig. 10 shows the Picard convergence for a setup with $N_{\text{load}} = 10$ in the sixth step, which is similar to the one presented in [46].

However, it is important to keep in mind that for some problems the degree of nonlinearity of the return-mapping equations is so high that the convergence radius of iteration scheme is reduced [11]. In such cases, improved initial guesses or an increased number of load steps is recommended [11,62]. Some researchers have also proposed more sophisticated algorithms [11,62,63] to improve convergence.

4.2.2. The plastic front position

The following set of analyses is dedicated to the study of the behaviour of hoop stresses (σ_θ) and axial stresses (σ_z) in Fig. 9. Neither of the two numerical solutions is able to accurately follow the analytical solution. Nevertheless, a zoomed in section of the hoop stress shows the breaking point, which is located at the elastic-plastic interface, indicating that the two conceptually different numerical solutions agree well. It seems that both numerical approaches overestimate the position of the plastic front by about 4 mm compared to the analytical solution (see also Table 3). A possible reason for this observed discrepancy between analytical and numerical solutions could lie in the derivation of the analytical solution, which was originally derived for the Tresca yielding criterion. The Tresca yielding theory[3] is known to be more conservative than the von Mises theory [64].

The position of the plastic front c is estimated using the numerical solution $\hat{u}$. Example demonstrating how the elastic-plastic interface has been determined is shown in Fig. 11. The red and blue dots mark the plastic and elastic regions respectively. To determine the position of the front, we fitted the following function to the computed data

$$f_{\text{fit}}(r) = C_1 r^{-1} + C_2 r^{-2} + C_3 \log(r^{-1}) + C_4 \tag{34}$$

with constants C_i (provided in Table 2) to fit the data and a continuous black line to represent them in Fig. 11. The intersection of the two fitted lines gives us an estimate of the position of the plastic front c. For the sake of clarity, only the analysis for the present solution procedure is shown in Fig. 11, while Table 3 also shows the numerical data for the FEM solution.

---

[3] From a design perspective, the Tresca yield condition is safer, but it also tempts the engineer to take unnecessary measures to prevent unlikely failure. Experiments indicate that the von Mises yield criterion shows a better agreement with the observed behaviour than the Tresca yield criterion. However, the Tresca yield criterion is still used due to its mathematical simplicity.
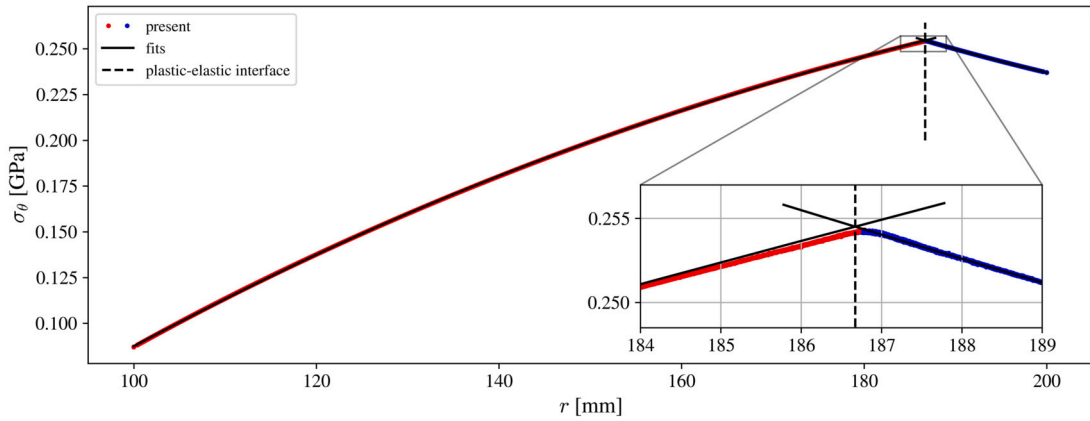
Fig. 11. Example of plastic-elastic interface determination. Blue dots represent the points where the accumulated plastic strain $\bar{\varepsilon}^p = 0$, and red dots $\bar{\varepsilon}^p > 0$.

Table 3
Results of the perfect plastic case - von Mises stress, and displacement magnitude at inner and outer surfaces, and position of the elastic-plastic interface. Under "Present" results we present the solution with $N \approx 95\,000$ vs. FEM vs. analytical approximation.

	σ_{VMS} [GPa]		$\|\mathbf{u}\|$ [mm]		c [mm]	N
	$r = a$	$r = b$	$r = a$	$r = b$		
Present	0.2400*	0.2106*	0.3623*	0.2053*	186.67☆	95 300
FEM	0.2400	0.2109	0.3593	0.2057	186.79☆	71 473
Analytical	0.2400△	0.2060	0.3546	0.2008	182.89	-

* Average for all nodes on the edge.
☆ Determined by fitting lines through points that are in the plastic zone ($\varepsilon^p > 0$), and points that are outside it ($\varepsilon^p = 0$), and finding the intersection between the two fits.
△ Presumed von Mises stress criterion.

Table 3 clearly shows that the two numerical solutions are in good agreement in terms of all studied variables. The von Mises stress in the two extreme parts of the domain, i.e. $r = a$ and $r = b$ are in good agreement. The displacement magnitude $\|\mathbf{u}\|$ shows a marginal difference, but the position of the plastic front c again differs by only a tenth of a millimetre. As already observed in Fig. 9, the analytic solution predicts the elastic-plastic interface to be about 4 mm closer to the origin.

4.2.3. Shape of the elastic-plastic front

Due to the cylindrical symmetry of the governing problem, the obtained numerical solution is expected to have symmetric properties. For example, the elastic-plastic front shape is expected to maintain a circular shape. Therefore, in this section, the front positioning algorithm from Section 4.2.2 is extended and applied to N_{seg} segments which divide the computational domain evenly. A schematic representation of the domain division is shown in Fig. 12 on the right-hand side, where a coarse domain discretization with $N = 6078$ is shown for clarity.

To determine the front position within each segment, the front position is estimated using the same procedure as in Section 4.2.2, with the difference that only the nodes within a specific segment are used, while the algorithm in Section 4.2.2 works with all computational nodes.

The shape of the front was computed for the finest domain discretization. The results for $N_{\mathrm{seg}} = 20$ segments with approximately 5000 nodes within each segment are shown in Fig. 12 in the centre. For reference, the fully symmetric FEM solution is added with a black line. The numerical solution obtained with the present approach indeed preserves the circular shape of the elastic-plastic front position. The circular shape is further evaluated in Fig. 12 on the right, where the distance of the plastic front from the origin r_{present} is compared with the distance r_{FEM} of the FEM-based solution.

4.3. Linearly-hardening yielding of an internally pressurized thick-walled cylinder

In this section, we consider the case of isotropic linear hardening in the plastic regime (see dotted red line in Fig. 1). Although pure linear hardening can hardly be observed in real materials, it forms strong foundations for the simulation of realistic materials. The hardening curve for real materials is usually measured experimentally during a uniaxial tensile test, where the experimental data is interpolated with a piecewise linear function to create a model that can be used in the numerical simulation.

Specifically, in our case, the hardening curve is defined as follows

$$\sigma_y(\bar{\varepsilon}^p) = 0.24\,\mathrm{MPa} + 10\,\mathrm{MPa} \cdot \bar{\varepsilon}^p, \tag{35}$$
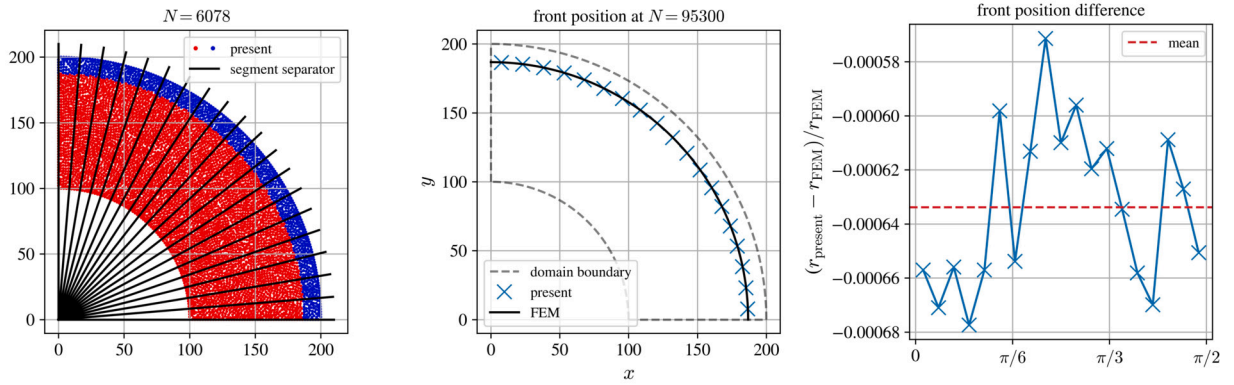
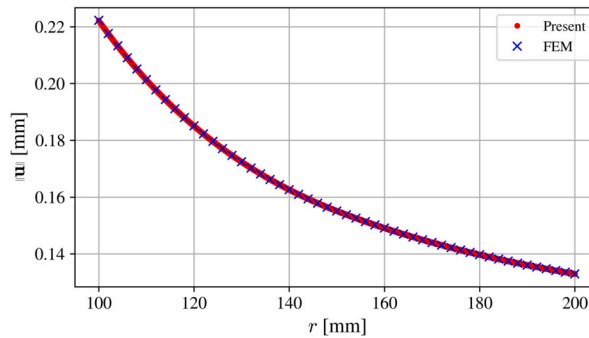**Fig. 12.** The elastic-plastic front distance to the origin computed for each of the $N_{\text{seg}} = 20$ segments.

Fig. 13. Displacement magnitude $\|\mathbf{u}\|$ vs radial coordinate r. Present solution compared with FEM. Note that the FEM solution is only displaying every second point for clarity.

Table 4
Results of the linear-hardening plastic case - von Mises stress, and displacement magnitude at inner and outer surfaces, and position of the elastic-plastic interface.

	σ_{VMS} [GPa]		$\|\mathbf{u}\|$ [mm]		c [mm]	N
	$r = a$	$r = b$	$r = a$	$r = b$		
Present	0.25589*	0.13635*	0.22212*	0.13295*	149.42☆	95 346
FEM	0.25592	0.13634	0.22224	0.13294	149.40☆	71 473
$\frac{\hat{u} - \hat{u}_{\text{FEM}}}{\hat{u}_{\text{FEM}}} \cdot 10^3$	-0.117	0.073	-0.540	0.075	0.134	-

* Average for all nodes on the edge.
☆ Determined numerically as explained in Section 4.2.2.

resulting in a constant hardening slope $H = 10\,\text{MPa}$ throughout the entire plastic regime.

Example solution fields obtained with the present solution procedure are similar to those shown in Fig. 7 and are therefore not shown again. Instead, the numerical solution obtained with the present method is compared with the community standard – the FEM solution of Abaqus. The Abaqus setup was the same as in the previous subsection. The two solutions are compared in terms of the displacement field magnitude with respect to the radial coordinate in Fig. 13. There is a good agreement between the two conceptually different approaches in the entire domain of radial coordinates. These observations are further confirmed by the numerical data in Table 4.

In the next step, we evaluate the accuracy of the numerical solution with respect to the secondary variables in Fig. 14. Note that the inside plot of Hoop stress σ_θ in Fig. 14 is a close-up to the breaking point, which is positioned at the plastic-elastic interface. All secondary variables also agree well with the FEM-based solution procedure.

A summary of the performance evaluation can be found in Table 4. We show the von Mises stresses and displacement magnitudes at both extremes of the domain, i.e. $r = a$ and $r = b$. In addition, the position of the plastic front c is shown. Note that the same procedure as in the previous Section 4.2.2 was used to determine the position of the plastic-elastic interface c, with the constants C_i summarised in Table 5.
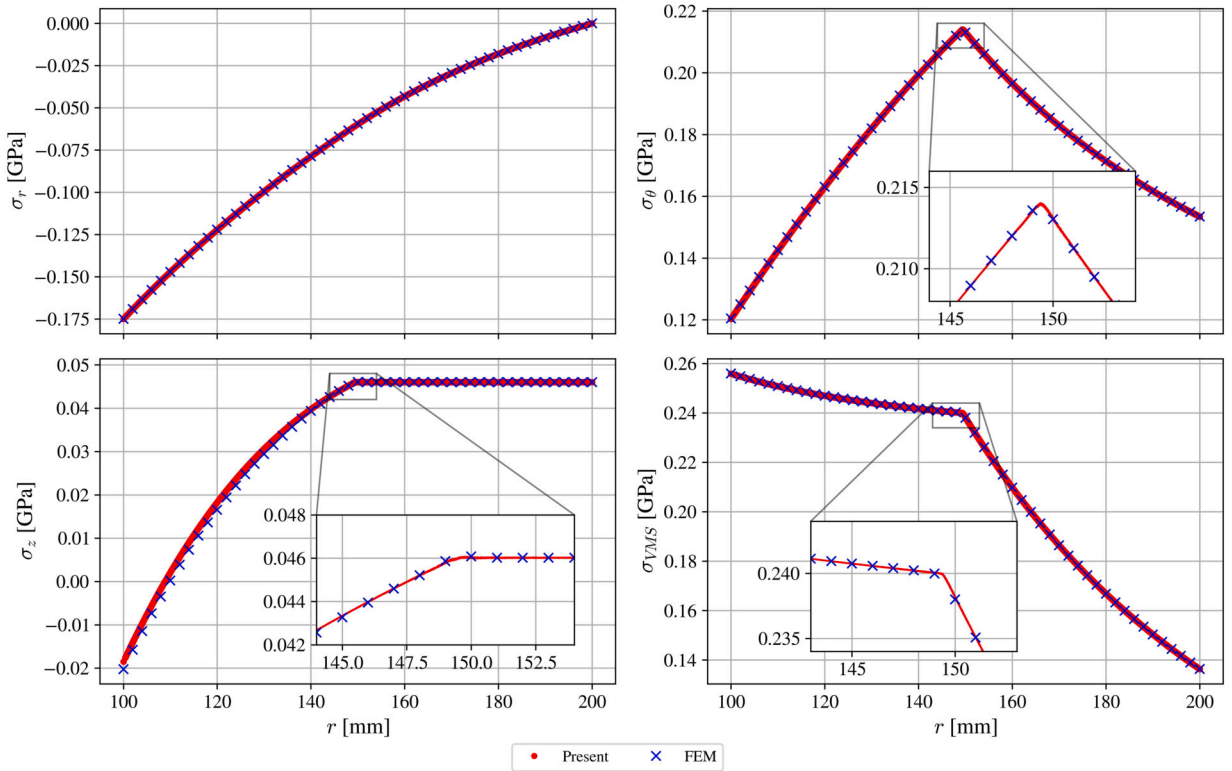
Fig. 14. Stress analysis in case of isotropic linear hardening.

Table 5
Constant values C_i used to determine the plastic front position c in case of linear hardening.

regime	C_1	C_2	C_3	C_4
plastic	$-8.120 \cdot 10^1$	$2.426 \cdot 10^3$	$1.016 \cdot 10^{-1}$	1.157
elastic	$2.993 \cdot 10^{-1}$	$3.055 \cdot 10^3$	$-8.508 \cdot 10^{-4}$	$7.102 \cdot 10^{-2}$

5. Additional example

In addition to already solved cases, we demonstrate a solution for irregular domain with a more realistic stress-strain relation. Additionally, the domain under consideration is cut with the following four spheres:

$$B_0 = \left\{ \mathbf{x} \in \mathbb{R}^2, \left\| \mathbf{x} - \frac{a+b}{2} \left(\cos\left(\frac{\pi}{16} \right), \sin\left(\frac{\pi}{16} \right) \right) \right\| < 20 \right\}, \tag{36}$$

$$B_1 = \left\{ \mathbf{x} \in \mathbb{R}^2, \left\| \mathbf{x} - \frac{a+b}{2} \left(\cos\left(\frac{7\pi}{16} \right), \sin\left(\frac{7\pi}{16} \right) \right) \right\| < 10 \right\}, \tag{37}$$

$$B_2 = \left\{ \mathbf{x} \in \mathbb{R}^2, \left\| \mathbf{x} - 0.8 \cdot a \left(\cos\left(\frac{\pi}{4} \right), \sin\left(\frac{\pi}{4} \right) \right) \right\| < 30 \right\}, \tag{38}$$

$$B_3 = \left\{ \mathbf{x} \in \mathbb{R}^2, \left\| \mathbf{x} - 1.1 \cdot b \left(\cos\left(\frac{\pi}{4} \right), \sin\left(\frac{\pi}{4} \right) \right) \right\| < 50 \right\}, \tag{39}$$

resulting in a domain as shown in Fig. 16. The edge of B_2 is subjected to internal pressure $p = 0.13\,\text{MPa}$, while the remaining three sphere edges are traction free, i.e. $\boldsymbol{\sigma} \vec{n} = 0$.

For the material properties, we simulate a set of uniaxial test results and use a piecewise linear interpolation in the solution procedure. The stress-strain relation is given as provided in Table 6 and illustrated in Fig. 15.

The domain is discretized with 20 292 scattered nodes corresponding to approximately 1 mm internodal spacing. Example solution is shown in Fig. 16 with displacement magnitudes on the left and accumulated plastic strain $\bar{\varepsilon}^p$ on the right. The proposed solution

Table 6

Synthetic stress-strain relation data.

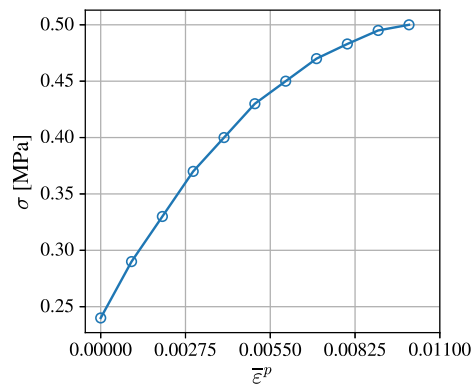| σ [MPa]	$\overline{\varepsilon}^p$
0.240	0.000
0.290	0.001
0.330	0.002
0.370	0.003
0.400	0.004
0.430	0.005
0.450	0.006
0.470	0.007
0.483	0.008
0.495	0.009
0.500	0.010

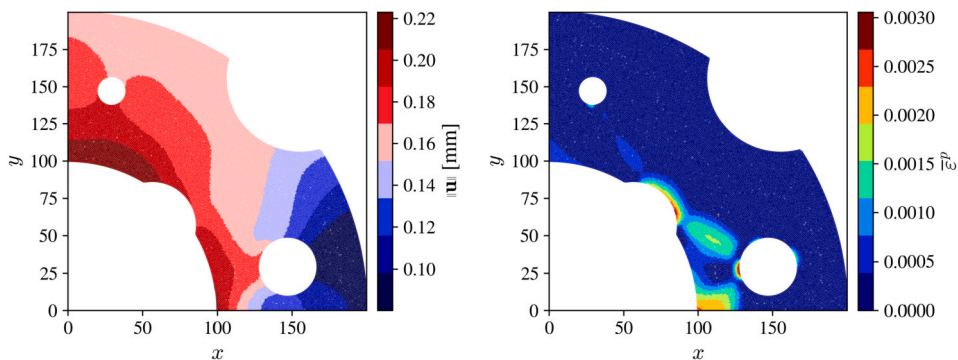**Fig. 15.** Plotted synthetic stress-strain relationship.

Fig. 16. Example solution on irregular domain. Displacement magnitude (left) and accumulated plastic strain (right).

procedure is clearly able to cope with irregular domains and real-like material properties. The largest plastic deformations are observed in the bottom right part of the domain, while the largest deformations are observed in the top right part of the domain, effectively yielding an ellipse-like deformed shape. Note that no special technique or algorithm adjustments were required to solve such problem. The solution procedure used is exactly as described in Algorithm 2.

6. Conclusions

This paper discusses the use of meshless methods, specifically RBF-FD, in solving an elasto-plastic problem using the Picard iteration. The study confirms that the presented solution method effectively accounts for different stages of material behaviour, from elastic deformation to perfect plastic yielding and linear hardening conditions. The method shows good agreement with analytical and FEM solutions (obtained with the commercial Abaqus solver), confirming its accuracy and robustness. It exhibits stable behaviour and provides results that are independent of the underlying geometry, without the need for special treatment in the approximation of differential operators, boundary conditions, or spatial discretization.

The performance of the proposed method is analyzed from various perspectives. To establish basic confidence in the proposed solution procedure, we first examined the purely elastic case and obtained the expected convergence properties and good agreement with the FEM solution. In the next step, perfectly plastic yielding was analyzed, also showing excellent agreement with the FEM solution. We also investigated the influence of N_{load} on solution accuracy and the convergence of the Picard iteration, showing that N_{load} has no significant effect on the final solution for the problem at hand. Further verification of the proposed method was performed by analyzing the shape of the plastic front, which again confirmed agreement with the FEM solution. In the final verification test, we compared the present solution with the FEM solution under isotropic linear hardening in the plastic region and again achieved good agreement.

The proposed iterative numerical algorithm initially assumes elastic deformation, i.e. in the first step, displacement and strain fields are calculated by solving the Navier-Cauchy equation. If the stress at any node exceeds the yield stress, indicating plastic deformation, a correction is made using a return mapping algorithm that adjusts the calculated stresses and strains to account for plastic effects. In contrast to the recent solution in [42], where the Newton-Raphson iteration was used to solve the system of nonlinear equations arising from plastic deformation, here we propose the use of Picard iteration. Picard iteration is a simpler approach that avoids assembling the Jacobian matrix and uses only elastic material parameters, resulting in a constant stiffness matrix during the iteration. Although such approach converges monotonically and is significantly slower than the Newton-Raphson iteration [46], it is way simpler to implement, it is less computationally expensive per iteration and, as shown in this paper, converges without stabilising the divergence operator or the boundary conditions. A direct consequence of this simplification is that the proposed approach allows the direct application of the method to complex geometries discretised with purely scattered nodes generated by the advancing front algorithm [18] that can be generalised to higher dimensions [48] and supports h-adaptive [31] spatially variable node spacing. In this paper, we demonstrate the ability of handling complex geometries by solving the case of a thick-walled cylinder with cut-outs.

While the presented meshless approach offers considerable potential advantages, it is not without drawbacks. Despite extensive research, the RBF-FD method still has some unsolved problems. Node quality in a meshless context is not nearly as well understood as meshes in FEM, where mesh quality measures such as aspect ratio, skewness, Jacobian ratio, etc. are well-defined concepts [65]. There are also no clear guidelines for the selection of stencils. In this work, we simply used the nearest n nodes as a stencil, which leads to a relatively computationally intensive method due to the rather high stencil size requirements [57].

Future work could focus on extending this method to three-dimensional problems and investigating the effects of dynamic loading conditions in more complex hardening models. As for the approximation method, symmetric stencils [66] could be used in addition to simple closest neighbourhood stencils, to improve the execution performance. The presented method is also compatible with the recently introduced h [31] and hp [32] adaptivities, which could be used to improve the performance of elasto-plastic deformation simulation. As for the iteration, an improved Picard iteration could be considered, which has been recently applied to flow in porous media [67]. The presented solution could also be coupled with a more sophisticated Newton-Raphson iteration to alleviate its stability problems [46].

CRediT authorship contribution statement

Filip Strniša: Writing – review & editing, Writing – original draft, Visualization, Software, Methodology, Investigation, Conceptualization. **Mitja Jančič:** Writing – original draft, Visualization, Methodology, Investigation. **Gregor Kosec:** Writing – original draft, Supervision, Project administration, Methodology, Investigation, Funding acquisition.

Declaration of competing interest

The authors declare that they have no known competing financial interests or personal relationships that could have appeared to influence the work reported in this paper.

Data availability

All data — including source code — is publicly available in git repository at https://gitlab.com/e62Lab/public/p_2d_plasticity under tag *v1.0*.

Acknowledgements

References

[1] J. Chakrabarty, Theory of Plasticity, McGraw-Hill International editions, Engineering Mechanics Series, McGraw-Hill, 1987.
[2] R. Hill, The Mathematical Theory of Plasticity, Oxford Classic Texts in the Physical Sciences, Clarendon Press, 1998.
[3] S. Timoshenko, History of Strength of Materials: With a Brief Account of the History of Theory of Elasticity and Theory of Structures, Courier Corporation, 1983.
[4] S. Eugster, Geometric Continuum Mechanics and Induced Beam Theories, Lecture Notes in Applied and Computational Mechanics, vol. 75, Springer, Cham, 2015.
[5] A.E.H. Love, G.H. Darwin, XVI. The small free vibrations and deformation of a thin elastic shell, Philos. Trans. R. Soc. Lond. A 179 (1888) 491–546, https://doi.org/10.1098/rsta.1888.0016, https://royalsocietypublishing.org/doi/pdf/10.1098/rsta.1888.0016, https://royalsocietypublishing.org/doi/abs/10.1098/rsta.1888.0016.

[6] O. Ozenda, E.G. Virga, On the Kirchhoff-Love hypothesis (revised and vindicated), J. Elast. 143 (2) (2021) 359–384, https://doi.org/10.1007/s10659-021-09819-7.

[7] V.A. Krysko, J. Awrejcewicz, M.V. Zhigalov, V.F. Kirichenko, A.V. Krysko, Mathematical models of higher orders, Shells in Temperature Fields (2019) 477.

[8] V. Krysko, J. Awrejcewicz, O. Saltykova, I. Papkova, A. Krysko, On the contact interaction of a two-layer beam structure with clearance described by kinematic models of the first, second and third order approximation, Mech. Syst. Signal Process. 115 (2019) 696–719.

[9] A. Krysko, J. Awrejcewicz, S. Pavlov, M. Zhigalov, V. Krysko, Chaotic dynamics of the size-dependent non-linear micro-beam model, Commun. Nonlinear Sci. Numer. Simul. 50 (2017) 16–28, https://doi.org/10.1016/j.cnsns.2017.02.015, https://www.sciencedirect.com/science/article/pii/S1007570417300631.

[10] C.K. Manoli, S. Papatzani, D.E. Mouzakis, Exploring the limits of Euler–Bernoulli theory in micromechanics, Axioms 11 (3) (2022), https://doi.org/10.3390/axioms11030142, https://www.mdpi.com/2075-1680/11/3/142.

[11] E.A. de Souza Neto, D. Peric, D.R.J. Owen, Computational Methods for Plasticity: Theory and Applications, Wiley, 2008.

[12] A.A. Roostaei, H. Jahed, A cyclic small-strain plasticity model for wrought mg alloys under multiaxial loading: numerical implementation and validation, Int. J. Mech. Sci. (2018).

[13] G.Y. Amouzou, A. Soulaïmani, Numerical algorithms for elastoplacity: finite elements code development and implementation of the Mohr–Coulomb law, Appl. Sci. 11 (10) (2021), https://doi.org/10.3390/app11104637.

[14] A.V. Krysko, J. Awrejcewicz, K.S. Bodyagina, M.V. Zhigalov, V.A. Krysko, Mathematical modeling of physically nonlinear 3D beams and plates made of multimodulus materials, Acta Mech. 232 (9) (2021) 3441–3469, https://doi.org/10.1007/s00707-021-03010-8, https://link.springer.com/10.1007/s00707-021-03010-8.

[15] B. Szabó, I. Babuška, Finite Element Analysis: Method, Verification and Validation, John Wiley & Sons, 2021.

[16] J. Gao, M. Xiao, Y. Zhang, L. Gao, A comprehensive review of isogeometric topology optimization: methods, applications and prospects, Chin. J. Mech. Eng. 33 (2020) 1–14.

[17] G.-R. Liu, Meshfree Methods: Moving Beyond the Finite Element Method, CRC Press, 2009.

[18] J. Slak, G. Kosec, On generation of node distributions for meshless pde discretizations, SIAM J. Sci. Comput. 41 (5) (2019) A3202–A3229, https://doi.org/10.1137/18M1231456.

[19] U. Duh, G. Kosec, J. Slak, Fast variable density node generation on parametric surfaces with application to mesh-free methods, SIAM J. Sci. Comput. 43 (2) (2021) A980–A1000.

[20] B. Fornberg, N. Flyer, Fast generation of 2-D node distributions for mesh-free PDE discretizations, Comput. Math. Appl. 69 (7) (2015) 531–544, https://doi.org/10.1016/j.camwa.2015.01.009.

[21] K. van der Sande, B. Fornberg, Fast variable density 3-d node generation, SIAM J. Sci. Comput. 43 (1) (2021) A242–A257.

[22] V. Shankar, R.M. Kirby, A.L. Fogelson, Robust node generation for meshfree discretizations on irregular domains and surfaces, SIAM J. Sci. Comput. 40 (4) (2018) 2584–2608, https://doi.org/10.1137/17m114090x.

[23] U. Duh, V. Shankar, G. Kosec, Discretization of non-uniform rational b-spline (nurbs) models for meshless isogeometric analysis, J. Sci. Comput. 100 (2) (2024) 51.

[24] X. Li, H. Dong, Error analysis of the meshless finite point method, Appl. Math. Comput. 382 (2020) 125326.

[25] M. Bagheri, M. Mohammadi, M. Riazi, A review of smoothed particle hydrodynamics, Computational Particle Mechanics 11 (3) (2024) 1163–1219.

[26] D. Mirzaei, K. Hasanpour, Direct meshless local Petrov–Galerkin method for elastodynamic analysis, Acta Mech. 227 (3) (2016) 619–632.

[27] O. Nikan, Z. Avazzadeh, A localisation technique based on radial basis function partition of unity for solving Sobolev equation arising in fluid dynamics, Appl. Math. Comput. 401 (2021) 126063.

[28] A. Tolstykh, D. Shirobokov, On using radial basis functions in a "finite difference mode" with applications to elasticity problems, Comput. Mech. 33 (1) (2003) 68–79.

[29] V. Bayona, N. Flyer, B. Fornberg, G.A. Barnett, On the role of polynomials in rbf-fd approximations: II. Numerical solution of elliptic pdes, J. Comput. Phys. 332 (2017) 257–273.

[30] Ö. Oruç, A strong-form local meshless approach based on radial basis function-finite difference (rbf-fd) method for solving multi-dimensional coupled damped Schrödinger system appearing in Bose–Einstein condensates, Commun. Nonlinear Sci. Numer. Simul. 104 (2022) 106042.

[31] J. Slak, G. Kosec, Adaptive radial basis function-generated finite differences method for contact problems, Int. J. Numer. Methods Eng. 119 (7) (2019) 661–686, https://doi.org/10.1002/nme.6067.

[32] M. Jančič, G. Kosec, Strong form mesh-free hp-adaptive solution of linear elasticity problem, Eng. Comput. (2023) 1–21.

[33] S. Le Borne, W. Leinen, Guidelines for rbf-fd discretization: numerical experiments on the interplay of a multitude of parameter choices, J. Sci. Comput. 95 (1) (2023) 8.

[34] I. Tominec, E. Breznik, An unfitted rbf-fd method in a least-squares setting for elliptic pdes on complex geometries, J. Comput. Phys. 436 (2021) 110283.

[35] Z. Ji-fa, Z. Wen-pu, Z. Yao, A meshfree method and its applications to elasto-plastic problems, J. Zhejiang Univ. Sci. A 6 (2) (2005) 148–154.

[36] M. Kargarnovin, H.E. Toussi, S. Fariborz, Elasto-plastic element-free Galerkin method, Comput. Mech. 33 (2004) 206–214.

[37] J. Belinha, M. Aires, D.E. Rodrigues, Elastoplastic analysis of frame structures using radial point interpolation meshless methods, Appl. Sci. 13 (23) (2023), https://doi.org/10.3390/app132312591, https://www.mdpi.com/2076-3417/13/23/12591.

[38] G. Kosec, J. Slak, M. Depolli, R. Trobec, K. Pereira, S. Tomar, T. Jacquemin, S.P. Bordas, M.A. Wahab, Weak and strong from meshless methods for linear elastic problem under fretting contact conditions, Tribol. Int. (2019), https://doi.org/10.1016/j.triboint.2019.05.041.

[39] M.A. Jankowska, On elastoplastic analysis of some plane stress problems with meshless methods and successive approximations method, Eng. Anal. Bound. Elem. 95 (2018) 12–24, https://doi.org/10.1016/j.enganabound.2018.06.013.

[40] P. Jiang, H. Zheng, J. Xiong, P. Wen, Nonlinear elastic-plastic analysis of reinforced concrete column-steel beam connection by rbf-fd method, Eng. Anal. Bound. Elem. 128 (2021) 188–194.

[41] J. Wang, G. Liu, On the optimal shape parameters of radial basis functions used for 2-d meshless methods, Comput. Methods Appl. Mech. Eng. 191 (23–24) (2002) 2611–2630.

[42] G. Vuga, B. Mavrič, B. Šarler, An improved local radial basis function method for solving small-strain elasto-plasticity, Comput. Methods Appl. Mech. Eng. 418 (2024) 116501, https://doi.org/10.1016/j.cma.2023.116501, https://linkinghub.elsevier.com/retrieve/pii/S0045782523006254.

[43] J.A. Kolodziej, M.A. Jankowska, M. Mierzwiczak, Meshless methods for the inverse problem related to the determination of elastoplastic properties from the torsional experiment, Int. J. Solids Struct. 50 (25) (2013) 4217–4225, https://doi.org/10.1016/j.ijsolstr.2013.08.025, https://www.sciencedirect.com/science/article/pii/S0020768313003417.

[44] F. Moayyedian, J.K. Grabski, Elastic–plastic torsion problem with non-linear hardenings using the method of fundamental solution, Arch. Civ. Mech. Eng. 21 (4) (2021) 155.

[45] B. Xu, R. Zhang, K. Yang, G. Yu, Y. Chen, Application of generalized finite difference method for elastoplastic torsion analysis of prismatic bars, Eng. Anal. Bound. Elem. 146 (2023) 939–950, https://doi.org/10.1016/j.enganabound.2022.11.028, https://www.sciencedirect.com/science/article/pii/S0955799722004295.

[46] V.M. Yarushina, M. Dabrowski, Y.Y. Podladchikov, An analytical benchmark with combined pressure and shear loading for elastoplastic numerical models, Geochem. Geophys. Geosyst. 11 (8) (2010), https://doi.org/10.1029/2010GC003130.

[47] H. Wendland, Scattered Data Approximation, vol. 17, Cambridge University Press, 2004.

[48] M. Jančič, J. Slak, G. Kosec, Monomial augmentation guidelines for rbf-fd from accuracy versus computational time perspective, J. Sci. Comput. 87 (1) (2021) 9.

[49] M. Najafi, M. Dehghan, B. Šarler, G. Kosec, B. Mavrič, Divergence-free meshless local Petrov–Galerkin method for Stokes flow, Eng. Comput. 38 (6) (2022) 5359–5377, https://doi.org/10.1007/s00366-022-01621-w, https://link.springer.com/10.1007/s00366-022-01621-w.

[50] J.M. Berljavac, P.K. Mishra, J. Slak, G. Kosec, RBF-FD analysis of 2D time-domain acoustic wave propagation in heterogeneous media, Comput. Geosci. 153 (2021) 104796.

[51] M. Jančič, M. Založnik, G. Kosec, Meshless interface tracking for the simulation of dendrite envelope growth, J. Comput. Phys. 507 (2024) 112973, https://doi.org/10.1016/j.jcp.2024.112973, https://linkinghub.elsevier.com/retrieve/pii/S0021999124002225.

[52] M. Depolli, J. Slak, G. Kosec, Parallel domain discretization algorithm for RBF-FD and other meshless numerical methods for solving PDEs, Comput. Struct. 264 (2022) 106773, https://linkinghub.elsevier.com/retrieve/pii/S0045794922000335.

[53] J. Slak, G. Kosec, Medusa: a C++ library for solving PDEs using strong form mesh-free methods, ACM Trans. Math. Softw. 47 (3) (2021) 1–25, https://doi.org/10.1145/3450966, https://dl.acm.org/doi/10.1145/3450966.

[54] O. Davydov, D.T. Oanh, Adaptive meshless centres and rbf stencils for Poisson equation, J. Comput. Phys. 230 (2) (2011) 287–304.

[55] O. Davydov, D.T. Oanh, N.M. Tuong, Improved stencil selection for meshless finite difference methods in 3d, J. Comput. Appl. Math. (2023) 115031.

[56] V. Bayona, Comparison of moving least squares and rbf+ poly for interpolation and derivative approximation, J. Sci. Comput. 81 (2019) 486–512.

[57] V. Bayona, An insight into rbf-fd approximations augmented with polynomials, Comput. Math. Appl. 77 (9) (2019) 2337–2353.

[58] N. Flyer, B. Fornberg, V. Bayona, G.A. Barnett, On the role of polynomials in rbf-fd approximations: I. Interpolation and accuracy, J. Comput. Phys. 321 (2016) 21–38.

[59] M. Jančič, G. Kosec, Stability analysis of rbf-fd and wls based local strong form meshless methods on scattered nodes, in: 2022 45th Jubilee International Convention on Information, Communication and Electronic Technology (MIPRO), 2022, pp. 275–280.

[60] J. Slak, G. Kosec, Refined meshless local strong form solution of Cauchy-Navier equation on an irregular domain, Eng. Anal. Bound. Elem. 100 (2019) 3–13, https://doi.org/10.1016/j.enganabound.2018.01.001, Improved Localized and Hybrid Meshless Methods - Part 1.

[61] G. Guennebaud, B. Jacob, et al., Eigen v3, http://eigen.tuxfamily.org, 2010.

[62] K. Krabbenhøft, Basic Computational Plasticity, University of Denmark, 2002.

[63] A. Perez-Foguet, A. Rodriguez-Ferran, A. Huerta, Consistent tangent matrices for substepping schemes, Comput. Methods Appl. Mech. Eng. 190 (35) (2001) 4627–4647, https://doi.org/10.1016/S0045-7825(00)00336-4, https://www.sciencedirect.com/science/article/pii/S0045782500003364.

[64] A.A. Roostaei, H. Jahed, 2 - fundamentals of cyclic plasticity models, in: H. Jahed, A.A. Roostaei (Eds.), Cyclic Plasticity of Metals, Elsevier Series on Plasticity of Materials, Elsevier, 2022, pp. 23–51.

[65] N.S. Gokhale, Practical Finite Element Analysis, Finite to Infinite, 2008.

[66] O. Davydov, D.T. Oanh, N.M. Tuong, Improved stencil selection for meshless finite difference methods in 3D, J. Comput. Appl. Math. 425 (2023) 115031, https://doi.org/10.1016/j.cam.2022.115031, https://linkinghub.elsevier.com/retrieve/pii/S037704272200629X.

[67] S. Zhu, L. Zhang, L. Wu, L. Tan, H. Chen, Application of improved Picard iteration method to simulate unsaturated flow and deformation in deformable porous media, Comput. Geotech. 166 (2024) 105979, https://doi.org/10.1016/j.compgeo.2023.105979, https://www.sciencedirect.com/science/article/pii/S0266352X2300736X.